

Noise studies with Crab Cavities in the SPS for
the HL-LHC project



Thesis submitted in accordance with the requirements of the
University of Liverpool for the degree of Doctor in Philosophy

by

Natalia Triantafyllou

Day Month Year

Abstract

Acknowledgments

List of Figures

4.1	Cross section view of the CC cryomodule [6]. It has a total length of 3 m [8] and at its core there are the two DQW cavities, which are illustrated with light green color.	8
4.2	Diagram of the SPS HT monitor [12]. The beam is passing through a straight stripline coupler which is followed by a 180°hybrid. This configuration provides the sum (Σ) and the difference (Δ) signal of the two electrodes.	11
4.3	Example difference and sum signals (top and bottom plots, respectively) from the HT monitor, in time scale, with respect to the longitudinal position within the bunch over several SPS revolutions, after the basic post processing (Ref. [12]) but before the baseline correction. The different colors indicate the signals from different turns (every 100 turns).	11
4.4	2D representation of example difference and sum signals with respect to the longitudinal position within the bunch obtained from the HT monitor over several SPS revolutions.	12
4.5	HT monitor baseline correction for the SPS CC tests. The baseline signal (blue dashed line) refers to the mean of the difference signals acquired before the CC - main RF synchronisation. The measured signal (blue solid line) corresponds to the mean of the difference signal acquired after the synchronisation. Last, the corrected signal (orange solid line) is obtained after subtracting the baselin from the measured signal.	13
4.6	HT acquisitions before and after the synchronisation of the SPS main RF with the CC.	13

4.7	Intra-bunch offset from the CC kick expressed in millimeters after the removal of the baseline.	14
4.8	CC voltage reconstruction from the HT monitor.	15
4.9	Demonstration of the crabbing from the HT monitor signal. CC voltage and sum signal (longitudinal line density) measured from the HT monitor (top) together with the density plot (bottom) which visualises the effect of the CC kick in the beam.	16
4.10	Demonstration of the sinusoidal fit on the HT monitor reading in order to obtain the CC parameters. A four-parameter sinusoidal fit is performed using Eq. (4.2) in order to obtain the amplitude, V_{CC} , the frequency, f_{CC} , the phase, ϕ_{CC} , and the voltage offset, k . The fit results, are given in the yellow box.	18
4.11	Phase scan with CC1 at 26 GeV. The sensitivity of the measured CC voltage (left) and its uncertainty (right) on the phase is studied. The error bars of the voltage, V_{CC} , indicate the uncertainty, ΔV_{CC} . The error bars of the uncertainty, ΔV_{CC} , and the phase, ϕ_{CC} , correspond to the error of the fit parameter (see Appendix A.2).	19
5.1	Demonstration of the sinusoidal fit on the HT monitor reading in order to obtain the CC parameters as described in Section 4.4. The fit results, are given in the yellow box. The measured voltage amplitude, V_{CC} , was found to be 0.99 MV while its uncertainty, ΔV_{CC} , was measured at 0.04 MV. The measured voltage value agrees well with the requested value of 1 MV.	22
5.2	Example amplitude (left) and phase (right) noise spectra measured with a spectrum analyzer E5052B [20] during the emittance growth studies with CCs in SPS. The noise spreads-out up to 10 kHz (grey dashed line) overlapping the first betatron sideband at ~ 8 kHz (green dashed line). The spikes at high frequencies correspond to the harmonics of the revolution frequency and are a result of the bunch crossing.	24

5.3	Sketch of the SPS rotational wire scanners [22]. The wire moves across the proton beam generating secondary particles which are then detecting by a scintillator and a photomultiplier. From the measured photomultiplier current the beam profile is reconstructed.	27
5.4	Vertical beam profile obtained from the BWS.41677.V instrument. The measured data points (light blue) are fitted with a four parameter gaussian (orange) to obtain the beam size. The calculated emittance and its uncertainty are also shown.	27
5.5	Bunch by bunch horizontal (top) and vertical (bottom) emittance evolution during the experiment on September, 15, 2018. The four different colors indicate the different bunches. The different applied noise levels are also shown while the moments when the noise level changed are indicated with the grey vertical dashed lines. The emittance growth rates along with their uncertainties for the seven different noise settings are displayed at the legend at the bottom of the plots.	31
5.6	Summary plot of the emittance growth study with CC noise in 2018. The transverse emittance growth rate, for the four bunches, is shown as a function of the different levels of applied noise.	32
5.7	Evolution of the beam in transverse and longitudinal planes during the CC noise induced emittance growth experiment. Top: Horizontal emittance growth measured with the SPS WS. Middle: Vertical emittance growth measured with the SPS WS. Bottom: Bunch length evolution measured with the ABWLM (small markers) and the Wall Current Monitor (bigger markers).	34
5.8	Longitudinal profiles (top) and relative bunch position with respect to the center of the RF bucket (bottom) acquired with the Wall Current Monitor. The acquisitions correspond to the times when the sudden jumps in the bunch length evolution are observed (see Fig. 5.7).	35
5.9	Intensity evolution as measured with ABWLM (smaller markers) and with the Wall Current Monitor (bigger markers) during the experiment with CC noise in 2018.	37

5.10	Summary plot of the emittance growth study with CC noise in 2018 focused on bunch 1 only. The measured emittance growth rate (blue) and the expected growths from the theoretical model (black) are shown as a function of the different levels of applied noise.	39
B.1	Sampling of the continuous signal $y(t)$ at a finite number of points N . The sampled signal is the discrete-time signal $y(n\Delta t)$ with Δt the sampling interval and n an integer such that $n \in [0, N - 1]$	54
B.2	Example of a signal sampled at discrete time intervals, and the corresponding discrete Fourier transform.	55
B.3	Power spectrum of $y = \sin(2\pi f t)$, $f = 50$ Hz.	57
B.4	Single-sided power spectrum of the signal shown in Fig. B.2(a).	58
B.5	Instantaneous voltage of an oscillator in the presence of (a) amplitude noise, (b) phase noise, and (c) both amplitude and phase noise.	60
B.6	Steps required to generate the sequence of noise kicks to be applied in the simulations from the measured noise spectrum.	64
B.7	Power spectral density computed from the time series ϕ_n produced from a measured power spectrum (black), compared with the original measured power spectrum (green).	65
B.8	Comparison between emittance growth found from simulations in Py-HEADTAIL and emittance growth expected from an analytical model [1]. The emittance growth is driven by amplitude and phase noise, with kicks in the simulations generated from a measured power spectrum.	67

List of Tables

1.1	Multipole errors from SPS non-linear model, at 270 GeV.	3
4.1	Crab Cavities design parameters for the SPS tests in 2018.	8
4.2	Parameters for computing the CC voltage from the example HT mon- itor measurements discussed in this chapter.	15
5.1	Main machine and beam parameters for the emittance growth studies with CCs in SPS in 2018.	23
5.2	Phase and amplitude noise levels injected in the CC RF system for the emittance growth studies of 2018. The listed values correspond to the average PSD values over a frequency range of ± 500 Hz around the first betatron sideband, f_b . The calculated effective phase noise for the pa- rameters of the first bunch are also listed.	26

List of Symbols

E_b	Energy
J_x	Horizontal particle action
J_y	Vertical particle action
f_{rev}	Revolution frequency
V_{RF}	Main RF voltage
f_{RF}	Main RF frequency
CC	Crab Cavity
V_{CC}	CC voltage
f_{CC}	CC frequency
ϕ_{CC}	CC phase
β_{CC}	Beta function at the CC
Q_x	Horizontal tune
Q_y	Vertical tune
Q_s	Synchrotron tune
D_x	Horizontal dispersion function
D_y	Vertical dispersion function
β	Relativistic beta
γ	Relativistic gamma (Lorenz factor)
N_b	Bunch intensity i.e. number of particles (here protons)
Q'_x	Horizontal first order chromaticity
Q'_y	Vertical first order chromaticity
σ_t	Rms bunch length
ϵ_x	Horizontal normalised emittance of the beam
ϵ_y	Vertical normalised emittance of the beam
ϵ_x^{geom}	Horizontal geometric emittance of the beam
ϵ_y^{geom}	Vertical geometric emittance of the beam
ΔQ_x^{rms}	Betatron horizontal rms tune spread
ΔQ_y^{rms}	Betatron vertical rms tune spread
α_{xx}	Horizontal detuning coefficient

0. List of Tables

α_{yy}	Vertical detuning coefficient
$\alpha_{xy} = \alpha_{yx}$	Cross-detuning coefficients

Contents

Abstract	iii
Acknowledgments	v
List of figures	ix
List of tables	x
List of symbols	xii
1 Introduction	1
1.1 The CERN accelerator complex	2
1.2 Crab Cavities for High-Luminosity LHC	2
1.3 Project objectives and thesis outline	2
1.4 General parameters of the studies	2
1.4.1 SPS optics	2
2 Basics of accelerator beam dynamics	4
2.1 Emittance	4
2.2 Action angle variables	4
3 Theory of Crab Cavity noise induced emittance growth	6
4 Calibration of the Crab Cavities for the SPS tests in 2018	7
4.1 Crab Cavities' installation in the SPS	7
4.2 Operational considerations	9
4.3 SPS Head-Tail monitor as the main diagnostic	9
4.3.1 General information	10

4.3.2	Post processing in the presence of Crab Cavities	11
4.3.3	Crab Cavity voltage reconstruction	14
4.3.4	Demonstration of crabbing with proton beams	15
4.4	Characterisation of measured Crab Cavity voltage	17
4.4.1	Definitions of the amplitude and the uncertainty of the measurement	17
4.4.2	Dependence of the crab cavity voltage and offset on the phase .	18
5	Experimental studies 2018: emittance growth from Crab Cavity noise	20
5.1	Experimental configuration and procedure	20
5.1.1	Preparatory experimental studies	21
5.1.2	Machine and beam configuration	21
5.1.3	Experimental procedure	23
5.2	Injected RF noise	23
5.3	Emittance growth measurements	25
5.3.1	SPS Wire Scanners	26
5.3.2	Experimental results	29
5.4	Bunch length and intensity measurements	32
5.4.1	ABWLM and Wall Current Monitor	33
5.4.2	Bunch length measurements	33
5.4.3	Longitudinal profile measurements	35
5.4.4	Intensity measurements	36
5.5	Comparison of measured transverse emittance growth with the theoretical predictions	36
5.6	Conclusions and outlook	38
6	Emittance growth studies 2018: Measurements and analysis	40
7	Investigation of the discrepancy	41
7.1	Sensitivity studies	41
7.2	b3b5b7 multiple errors	41
8	Simple model of describing the decoherence suppression from impedance	42
9	Application and impact for HL-LHC	43

10 Conclusion	44
A Definitions and methods of statistical analysis	45
A.1 Basic terminology	45
A.1.1 Averages	45
A.1.2 Measuring the spread	46
A.1.3 Data sets with more than one variables - Covariance	47
A.2 Least squares fitting	47
A.3 Propagation of uncertainty	48
A.4 Detuning with amplitude	49
B Fundamentals of signal analysis and measurement	52
B.1 Continuous-time analysis	52
B.2 Discrete-time analysis	54
B.3 Measuring amplitude and phase noise	59
B.4 Applying a measured noise spectrum in numerical simulations	61
B.4.1 Crab cavity noise in numerical simulations	61
B.4.2 Measured noise spectrum	62
B.4.3 Generating time series	62
B.4.4 Validation of the time series reconstruction	65
C Glossary and defintions	68
Bibliography	72

1 | Introduction

This is the introduction of my PhD thesis.

1. General about standard model (Sofia, Schenk) 2. Role of CERN 3. Role of my thesis.

1.1 The CERN accelerator complex

1.2 Crab Cavities for High-Luminosity LHC

1.3 Project objectives and thesis outline

Probably put to abstract

In 2018, two prototype Crab Cavities (CCs) were installed in the SPS to be tested for the first time with proton beams. A series of dedicated machine development studies was carried out in order to validate their working principle and answer various beam dynamic questions. One of the operational issues that needed to be addressed concerned the expected emittance growth due to noise in their RF system, which is the main subject of this thesis. As mentioned in chapter 3 a theoretical model had already been developed and validated by tracking simulations [1]. As a part of the first experimental campaign with CCs in SPS a dedicated experiment was conducted to benchmark these models with experimental data and confirm the analytical predictions. The objective of this chapter is to provide an overview of the machine setup for the CC experiments and introduce the instruments and methods used for measuring the beam parameters of interest for the emittance growth studies.

1.4 General parameters of the studies

1.4.1 SPS optics

The studies presented in this thesis were performed for the nominal SPS optics for the LHC filling which are called Q26 optics as the higher integer part of the tune in both planes is 26.

SPS nominal model

The model for the Q26 optics can be found in the official CERN repository [2] and

will be referred to as the nominal SPS model in this thesis. The values of the optics parameters in what follows correspond to the model values unless stated otherwise.

SPS non-linear model

The nominal SPS model includes only the nonlinear fields produced by the chromatic sextupoles. However, one of the most important sources of non-linearities in SPS are the odd multipole components of its main dipole magnets. For some of the studies presented in this thesis their impact on the beam dynamics must be studied and therefore they should be included in the nominal model.

The multipole error of the SPS main dipoles are unfortunately not available from magnetic measurements. On this ground a non-linear optics model of the SPS has been established with beam-based measurements of the chromatic detuning over a range of momentum deviation [3, 4]. The optics model was obtained by assigning systematic multipole components to the main lattice magnets, in the nominal model of SPS, in order to reproduce the tune variation with themomentum deviation as it was measured in the real machine. The calculations were performed with MAD-X [].

The values of the multipole components up to seventh order obtained from this method are given in Table 1.1 where, (b_3^A, b_3^B) (b_5^A, b_5^B) and (b_7^A, b_7^B) stand for the sextupolar, decapolar and decatetrapolar mutipoles respectively. Note that different values have been obtained foreach of the two different kinds of SPS main dipoles (MBA and MBB) which are marked withthe indices A and B respectively.

Table 1.1: Multipole errors from SPS non-linear model, at 270 GeV.

Multipole	Value
b_3^A, b_3^B	$8.1 \times 10^{-4} \text{ m}^{-2}, 1.1 \times 10^{-3} \text{ m}^{-2}$
b_5^A, b_5^B	$9.2 \text{ m}^{-4}, -10 \text{ m}^{-4}$
b_7^A, b_7^B	$1.3 \times 10^5 \text{ m}^{-6}, 1.4 \times 10^5 \text{ m}^{-6}$

random multiple erros? Like in APR.Ch.3.2.2.

2 | Basics of accelerator beam dynamics

2.1 Emittance

Defintion 1: The statistical emittance is expressed in terms of the beam distribution:

$$\epsilon_x^{\text{geom}} = \sqrt{\langle x^2 \rangle - \langle px \rangle^2}. \quad (2.1)$$

This is the geometric emittance.

$$\epsilon_x = \epsilon_x^{\text{geom}} \beta \gamma. \quad (2.2)$$

Defintion 2: For a gaussian beam distribution the normalised beam emittance it applies:

$$\epsilon_x = \frac{\sigma_x(s)^2 - \delta^2 D_x^2(s)}{\beta_x(s)} \beta \gamma \quad (2.3)$$

where $\sigma_x(s)$ is the beam size, $\beta_x(s)$ is the beta function, $D_x(s)$ is the dispersion fat a specific location s along the accelerator, $\delta = \Delta p / p_0$ is the momentum spread and β, γ the relativistic parameters. Similar expression is valid for the vertical plane, with the difference that there is no dispersion.

2.2 Action angle variables

The action for the x-plane is:

$$J_x = \frac{1}{2} (x_n^2 + x p_n^2) \quad (2.4)$$

where

$$x_n = \frac{x}{\sqrt{\beta_x}}, \quad xp_n = \frac{\alpha_x x}{\sqrt{\beta_x}} + \sqrt{\beta_x} xp \quad (2.5)$$

the normalised coordinates and α_y, β_y the twiss parameters. The same applies for the y-plane.

The statistical geometric emittance equals the average of the actions distribution:

$$\epsilon_x^{geom} = \langle J_x \rangle \quad (2.6)$$

The distribution of actions is an exponential distribution (further explanation needed?).

Therefore, its mean equals its standard deviation. (this property is used in the appendix for the computation of the rms tune spread.)

From Eq. (2.4) we write:

$$e^{-J/\epsilon} = e^{(-x^2/2\epsilon - px^2/2\epsilon)} \quad (2.7)$$

From this equation it can be seen that the actions follow an exponential distribution.

3 | Theory of Crab Cavity noise induced emittance growth

For a uniform noise spectrum across the betatron tune distribution, the emittance growth resulting from amplitude noise can be estimated from:

$$\frac{d\epsilon}{dt} = \beta_{CC} \left(\frac{eV_{CC}f_{rev}}{2E_b} \right)^2 C_{\Delta A}(\sigma_\phi) \sum_{k=-\infty}^{+\infty} S_{\Delta A}[(k \pm \bar{\nu}_b \pm \bar{\nu}_s)f_{rev}]. \quad (3.1)$$

For phase noise, the emittance growth can be estimated from:

$$\frac{d\epsilon}{dt} = \beta_{CC} \left(\frac{eV_{CC}f_{rev}}{2E_b} \right)^2 C_{\Delta\phi}(\sigma_\phi) \sum_{k=-\infty}^{+\infty} S_{\Delta\phi}[(k \pm \bar{\nu}_b)f_{rev}]. \quad (3.2)$$

In these formulae, β_{CC} is the beta function at the location of the CC, V_{CC} the CC voltage, f_{rev} the revolution frequency of the beam, E_b the beam energy, and $\bar{\nu}_b$ and $\bar{\nu}_s$ the mean of the betatron and synchrotron tune distribution. $S_{\Delta A}$ and $S_{\Delta\phi}$ are the power spectral densities (PSD) [5] of the noise at all the betatron and synchrobetatron (for the amplitude noise case) sidebands. $C_{\Delta A}$ and $C_{\Delta\phi}$ are correction terms to account for the bunch length:

$$C_{\Delta A}(\sigma_\phi) = e^{-\sigma_\phi^2} \sum_{l=0}^{+\infty} I_{2l+1}(\sigma_\phi^2), \quad (3.3)$$

$$C_{\Delta\phi}(\sigma_\phi) = e^{-\sigma_\phi^2} \left[I_0(\sigma_\phi^2) + 2 \sum_{l=1}^{+\infty} I_{2l}(\sigma_\phi^2) \right], \quad (3.4)$$

with σ_ϕ the rms bunch length (in radians) with respect to the CC frequency f_{CC} , and $I_n(x)$ the modified Bessel function of the first kind.

4 | Calibration of the Crab Cavities for the SPS tests in 2018

In 2018 the CC technology was tested with proton beams in the SPS for the first time. In this chapter, the setup and the calibration of the CCs in the SPS are presented along with the demonstration of the first crabblings of proton beams. The objective is to provide a full understanding of the operational aspects of the CCs in the SPS and explain the measurement of the CC voltage which is one of the most crucial parameters for the emittance growth studies (see Chapter 3, Eq. (3.1) and Eq. (3.2)).

The chapter is structured as follows: Section 4.1 describes the installation of the CC system in the SPS. Thereafter, Section 4.2 elaborates on details for their operation in the SPS machine. In Section 4.3, the use of the Head-Tail (HT) monitor as the main diagnostic in the CC tests is discussed, focusing on the reconstruction of the CC voltage from its reading. Last, Section 4.4 provides a characterisation of the beam based CC voltage measurement and defines the voltage amplitude and its uncertainty.

4.1 Crab Cavities' installation in the SPS

For the SPS tests two prototype CCs of the Double Quarter Wave (DQW) type, which will be referred to as CC1 and CC2 through this thesis, were fabricated by CERN and were assembled in the same cryomodule, shown in Fig. 4.1 [6]. For its installation an available space was found at the SPS Long Straight Section 6 (SPS-LSS6) zone. As this section is also used for the extraction of the beam to the LHC, the cryomodule was placed on a mobile transfer table [7] which moved the cryomodule in the beam-

4. Calibration of the Crab Cavities for the SPS tests in 2018

line for the CC tests and out of it for the usual SPS operation without breaking the vacuum.



Figure 4.1: Cross section view of the CC cryomodule [6]. It has a total length of 3 m [8] and at its core there are the two DQW cavities, which are illustrated with light green color.

The main CCs parameters are listed in Table 4.1. Their location along the SPS ring is also indicated, in case someone would like to repeat the analysis described in this thesis.

Table 4.1: Crab Cavities design parameters for the SPS tests in 2018.

Parameter	Value	
	CC1	CC2
crabbing plane	vertical	vertical
s-location*	6312.72 m	6313.32 m
CC voltage, V_{CC}	≤ 3.4 MV	≤ 3.4 MV
CC frequency, f_{CC}	400.78 MHz	400.78 MHz
Horizontal / Vertical beta function, $\beta_{x,CC} / \beta_{y,CC}$	29.24 m / 76.07 m	30.31 m / 73.82 m
Horizontal / Vertical alpha function, $\alpha_{x,CC} / \alpha_{y,CC}$	-0.88 m / 1.9 m	-0.91 m / 1.86 m
Horizontal / Vertical dispersion, $D_{x,CC} / D_{y,CC}$	-0.48 m / 0 m	-0.5 m / 0 m

* The s-location is referred to the location of the elements along the SPS ring with respect to the start of the lattice i.e. element QF10010 which is a focusing quadrupole.

4.2 Operational considerations

For the beam tests with CCs in the SPS the approach regarding the energy ramp and the adjustment of the phasing with the main RF system needed to be evaluated and they are briefly discussed here.

Energy ramp

SPS receives the proton beam at 26 GeV from the PS. It was found that the ramp to higher energies could not be performed with the CC on, as the beam was getting lost while crossing one of the vertical betatron sidebands due to resonant excitation [9]. Therefore, it was established that the acceleration has to be performed with the CC off and its voltage must be set up only after the energy of interest has been achieved. It is worth noting that this approach will also be used in the HL-LHC.

Crab Cavity - main SPS RF synchronisation

It was important to ensure that during the "coast" the beam will experience the same kick from the CC each turn. In other words the SPS main RF system operating at 200 MHz needed to be synchronous with the CC operating at 400 MHz. Due to the larger bandwidth of the SPS main RF system the CC was used as a master. Therefore the CC was operating at a fixed frequency and phase, while the main accelerating cavities were adjusted to the exact half of the CC frequency and were re-phased so that they become synchronous with the crabbing signal. For the studies at higher energies the synchronisation took place at the end of the ramp shortly after the cavity was switched on [10].

4.3 SPS Head-Tail monitor as the main diagnostic

The SPS is equipped with a high bandwidth pick-up of approximately 2 GHz allowing to resolve the intra-bunch motion. This instrument is called Head-Tail (HT) monitor and was originally designed for measuring chromaticity and transverse instabilities. However, in the SPS CC tests, the HT monitor was the main diagnostic device deployed for the demonstration of the crabbing and the measurement of the CC voltage (explained in details in Section 4.4). Therefore its use as a crabbing diagnostic should be explained here. The methods and procedures described in this

section were developed at CERN and they are described here for the completeness of the thesis.

In the first part of this section some general information on the instrument along with example signals will be presented. Subsequently, the post processing of the HT signal in the presence of the CC will be discussed. Last, the calibration of the CC voltage from the HT data is described and the visualisation of the crabbing is displayed. The experimental data presented in this section were acquired, on May 30, 2018 (time-stamp: 13:51:05), at the SPS injection energy of 26 GeV with only one CC, CC1, at phase $\phi_{CC} = 0$ for simplicity. That energy of 26 GeV was chosen to provide a better understanding of the methods used as the orbit shift from the CC kick is stronger and thus more visible than in higher energies.

4.3.1 General information

As already mentioned, the HT monitor is a high bandwidth version of a standard beam position monitor, which means that it can measure the transverse displacement within the bunch. This makes it ideal for the measurement of the intra-bunch offset caused from the CC kick. Its reading consists of the sum (Σ) and the difference (Δ) of the electrode signals of a straight stripline coupler (Fig. 4.2) [11, 12] over a defined acquisition period. The sum signal is the longitudinal line density while the difference signal corresponds to the intra-bunch offset. The system operates at time scale where the signals are given as a function of the position within the bunch.

The raw signals from the HT monitor require a specific post-processing procedure, which is described in Ref. [12], in order to give useful information. Figure 4.3 shows some example signals obtained from the HT monitor after the basic post-processing is applied. Moreover, Fig. 4.4 shows a 2D representation of the HT monitor reading. It is worth noting here that in the specific example a clear modulating pattern in time of the vertical intra-bunch offset (vertical Δ) signal is observed. This is a result of the phase slip between the CC and the main RF system because they are not yet synchronised.



Figure 4.2: Diagram of the SPS HT monitor [12]. The beam is passing through a straight stripline coupler which is followed by a 180° hybrid. This configuration provides the sum (Σ) and the difference (Δ) signal of the two electrodes.

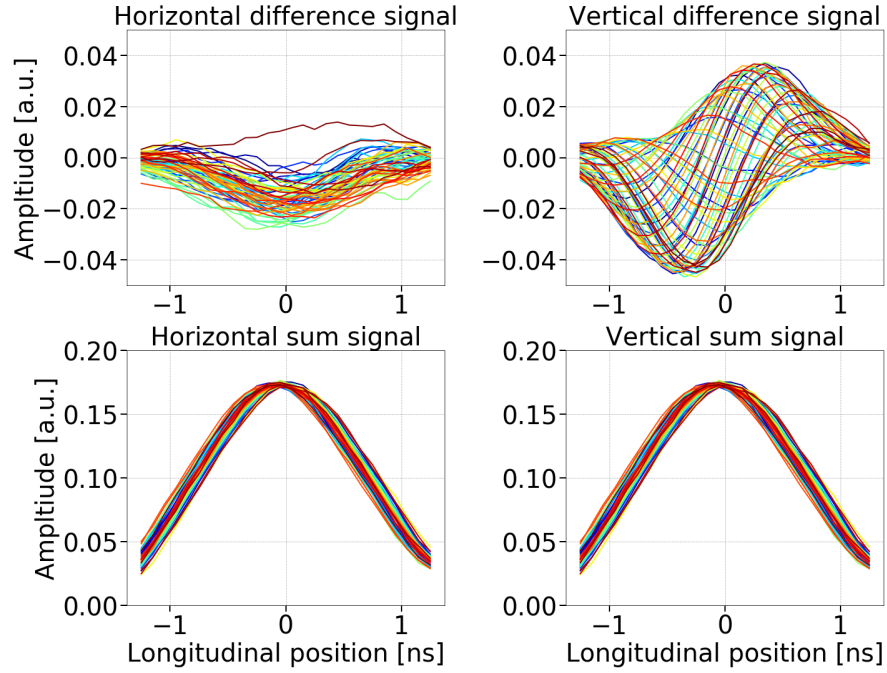


Figure 4.3: Example difference and sum signals (top and bottom plots, respectively) from the HT monitor, in time scale, with respect to the longitudinal position within the bunch over several SPS revolutions, after the basic post processing (Ref. [12]) but before the baseline correction. The different colors indicate the signals from different turns (every 100 turns).

4.3.2 Post processing in the presence of Crab Cavities

To obtain useful information from the HT monitor signal in the presence of the CCs there are a few steps that differ from the standard post processing procedure and they are described below.



Figure 4.4: 2D representation of example difference and sum signals with respect to the longitudinal position within the bunch obtained from the HT monitor over several SPS revolutions.

Head-Tail monitor baseline correction

The HT monitor measurement has a baseline on the difference signal which needs to be removed. The baseline is a result of orbit offsets and non-linearities of the instrument and is constant from turn to turn [12]. Therefore, during the normal post processing procedure (without CCs), the baseline is computed as the mean of the difference signals over all turns and then the correction is achieved by subtracting this static offset from the signal of each turn. However, in the SPS tests, where the CCs are well synchronised with the main RF system (Section 4.2), the crabbing signal is also a static intra-bunch position offset and thus would also be removed with the usual method. Because of technical limitations it was not feasible to switch off the CC for those kind of measurements. Thus, the following technique was used.

For the CC experiments a reference measurement had first to be made with the CC not being synchronous with the main RF system. The baseline was computed as the mean of the difference signals over this reference period and subsequently it

was subtracted from the average of the difference signals acquired after the synchronisation (Fig 4.5). The datasets before and after synchronisation are easily distinguishable in the 2D HT monitor reading as displayed in Fig. 4.6



Figure 4.5: HT monitor baseline correction for the SPS CC tests. The baseline signal (blue dashed line) refers to the mean of the difference signals acquired before the CC - main RF synchronisation. The measured signal (blue solid line) corresponds to the mean of the difference signal acquired after the synchronisation. Last, the corrected signal (orange solid line) is obtained after subtracting the baseline from the measured signal.



Figure 4.6: HT acquisitions before and after the synchronisation of the SPS main RF with the CC.

Head-Tail monitor scaling

The last step to make the HT acquisitions meaningful is to convert the measured intra bunch offset, mean of the difference signals after the CC - main RF synchronisation and after the baseline correction, from arbitrary units to millimeters. The

scaling is achieved by division with the mean of the sum signals after the synchronisation and with a normalisation factor which is provided by the calibration of the HT monitor [13]. The normalisation factor for the SPS was measured at 0.1052 in 2018 [14]. Figure 4.7 shows the intra-bunch offset from the CC kick in millimeters and after the baseline correction.



Figure 4.7: Intra-bunch offset from the CC kick expressed in millimeters after the removal of the baseline.

4.3.3 Crab Cavity voltage reconstruction

This section discusses the reconstruction of the CC voltage from the HT monitor signal. First, Eq. (4.1) was used to calculate the CC kick, θ , required to reconstruct the measured intra-bunch offset. Equation (4.1), which is obtained from Eq. (1) from chapter 4.7.1 in Ref. [15], gives the vertical orbit shift (in meters) from the CC kick, θ , at the HT monitor location as follows:

$$\Delta y_{HT} = \frac{\sqrt{\beta_{y,HT}}}{2 \sin(\pi Q_y)} \theta \sqrt{\beta_{y,CC}} \cos(\pi Q_y - |\psi_{y,HT} - \psi_{y,CC}|), \quad (4.1)$$

where β_y is the beta function, Q_y is the tune, and $|\psi_{y,HT} - \psi_{y,CC}|$ between the CC and the HT monitor in tune units. The same applies for the horizontal plane. The subscripts HT and CC indicate quantities at the location of the HT monitor and CC respectively.

The CC voltage is then reconstructed from the CC kick which is written as $\theta = -\frac{qV_{CC}(t)}{E_b}$,

where q is the charge of the particle, E_b the beam energy and $V_{CC}(t) = V_{CC} \sin(2\pi f_{CC} t + \phi_{CC})$ is the voltage that a particle experiences while passing through the CC. In the context where the HT monitor measures the signal as a function of time, t , the voltage in the above formula is expressed accordingly as $V_{CC}(t)$, where $t = 0$ the center of the bunch.



Figure 4.8: CC voltage reconstruction from the HT monitor.

It should be noted here, that the measured intra-bunch offset, Δy_{HT} , is inserted in Eq. (4.1) after removing the baseline and converting it to millimeters as discussed in Section 4.3.2. Figure 4.8 illustrates the cavity voltage computed from the HT signals shown already in this section. The corresponding beam and optic parameters are listed in Table 4.2.

Table 4.2: Parameters for computing the CC voltage from the example HT monitor measurements discussed in this chapter.

Parameter	Value
Beta function at the HT monitor, $\beta_{y,HT}$	49.19 m
Phase advance between the start* of the lattice and the HT monitor, $\psi_{y,HT}$	$15.68 \times 2\pi$
Beta function at the CC1, $\beta_{y,CC1}$	76.07 m
Phase advance between the start* of the lattice and CC1, $\psi_{y,CC1}$	$23.9 \times 2\pi$
Vertical betatron tune, Q_y	26.13
Beam energy, E_b	26 GeV

* The start of the lattice is considered the element QF10010 which is a focusing quadrupole.

4.3.4 Demonstration of crabbing with proton beams

Additionally, the measurements from the HT monitor were used for reconstructing the crabbing and representating schematically the beam projection **in the trans-**

verse plane. The technique for reconstructing the crabbing was developed at CERN in 2018 and was extensively used through the experimental campaign with CCs since (together with the calibrated voltage) it gives a straightforward estimate of the applied CC kick, as illustrated in Fig. 4.9.

To obtain this schematic representation, which is practically a density plot, of the effect of the CC kick on the beam one needs to multiply the measured longitudinal profile, mean of the sum signals acquired after the synchronisation, with the measured intra-bunch offset, mean of the difference signals acquired after the synchronisation. An example of this is shown in Fig. 4.7. For the transverse plane a gaussian distribution is considered with σ obtained from the wire scanner (addressed in more detail in the following section). The color code of Fig. 4.9 is normalised to the maximum intensity within the bunch.

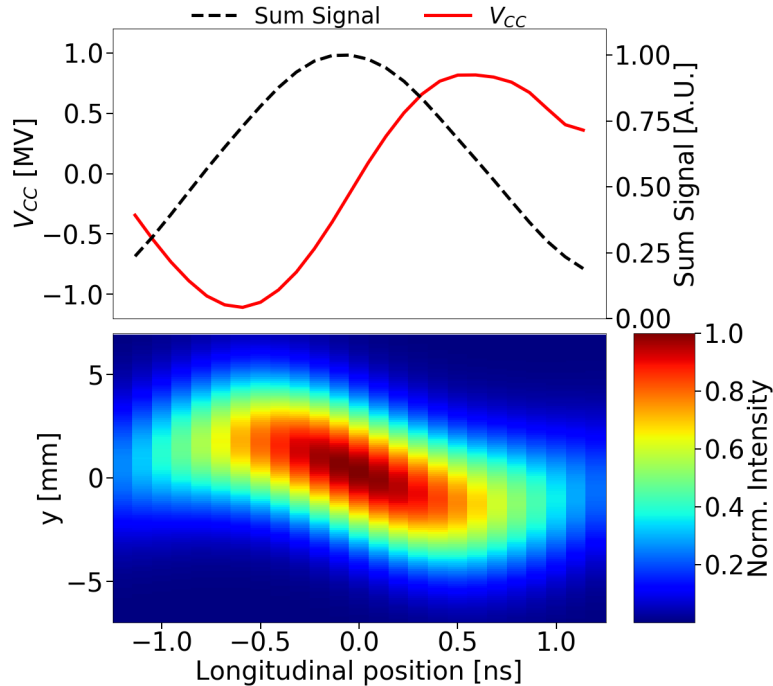


Figure 4.9: Demonstration of the crabbing from the HT monitor signal. CC voltage and sum signal (longitudinal line density) measured from the HT monitor (top) together with the density plot (bottom) which visualises the effect of the CC kick in the beam.

4.4 Characterisation of measured Crab Cavity voltage

This section gives the definitions of the amplitude of the beam-based measurement of the CC voltage and its uncertainty that will be used in this thesis. Additionally, their dependence on the CC phase is discussed for completeness.

4.4.1 Definitions of the amplitude and the uncertainty of the measurement

The voltage amplitude, V_{CC} , is obtained from a sinusoidal fit on the reconstructed voltage, $V_{CC}(t)$, from the HT monitor reading. The standard procedure of least squares fitting (see Appendix section A.2) is followed. In particular, $V_{CC}(t)$ is fitted with the following three-parameter (V_{CC} , ϕ_{CC} , k) model function which also provides the CC phase and voltage offset:

$$f(x) = V_{CC} \sin(2\pi f_{CC}x + \phi_{CC}) + k, \quad (4.2)$$

where V_{CC} is the amplitude of the CC voltage, ϕ_{CC} the CC phase and k the voltage offset. The fit is performed for a fixed CC frequency, as the operational value is well known and in particular it equals, $f_{CC}=400.78$ MHz. The offset parameter is added to the model function as it is clear from Fig. 4.8 and 4.9 that the reconstructed CC voltage, $V_{CC}(t)$, is not centered around zero.

In order to obtain results that correspond to the experimental conditions the following constraints are imposed to the fit. First the voltage amplitude, V_{CC} , is requested to always be positive and higher than 0.7 MV. Furthermore, the part of the signal that corresponds to the tails of the bunch is excluded from the fit in order not to degrade its quality. Subsequently, only the part of the signal for which the corresponding normalised sum signal is above 0.4 is used for the fit.

Fig. 4.10 shows the fit's result of the same signal that was analysed in the previous section. As indicated on the top of the plot, the red solid line corresponds to the reconstructed CC voltage, while the blue solid line corresponds to the result of the sinusoidal fit. It can be seen that only the part of the signal for which the normalised

sum signal (black dashed line) is above 0.4 is used. Finally the blue dashed line shows the result of the fit after the voltage offset is subtracted, such as it is centered around zero. The parameter values obtained from the fit are given in the legend. Last, the density plot is also shown at the bottom of the figure for a complete visualisation of the crabbing.



Figure 4.10: Demonstration of the sinusoidal fit on the HT monitor reading in order to obtain the CC parameters. A four-parameter sinusoidal fit is performed using Eq. (4.2) in order to obtain the amplitude, V_{CC} , the frequency, f_{CC} , the phase, ϕ_{CC} , and the voltage offset, k . The fit results, are given in the yellow box.

In this thesis, the uncertainty on the measured voltage amplitude, ΔV_{CC} is defined as the absolute value of the voltage offset, k , instead of the error of the fit on the voltage amplitude. This is because, the voltage offset depicts better the uncertainty of the voltage seen by the beam, V_{CC} . Therefore, for the analyzed example here the CC voltage was measured to be $V_{CC} = 0.98$ MV and its uncertainty $\Delta V_{CC} = 0.12$ MV.

4.4.2 Dependence of the crab cavity voltage and offset on the phase

The impact of the CC phase on the voltage experienced by the beam and on the uncertainty of its measurement was also studied experimentally. The study was performed on May 30, 2018, at the SPS injection energy of 26 GeV for a range of different

settings of the phase of CC1. The results are summarised in Fig. 4.11.



Figure 4.11: Phase scan with CC1 at 26 GeV. The sensitivity of the measured CC voltage (left) and its uncertainty (right) on the phase is studied. The error bars of the voltage, V_{CC} , indicate the uncertainty, ΔV_{CC} . The error bars of the uncertainty, ΔV_{CC} , and the phase, ϕ_{CC} , correspond to the error of the fit parameter (see Appendix A.2).

The error bars of the voltage, V_{CC} , indicate the uncertainty, ΔV_{CC} . The error bars of the uncertainty, ΔV_{CC} (left), and the phase, ϕ_{CC} (right), correspond to the error of the fit parameter (see Appendix A.2). It should be noted that the error bars on the phase values are smaller than the markers and are hence not visible in the plots.

The phase scan doesn't reveal any dependence of the measured voltage, V_{CC} , on the phase, as expected. However, there is a variation of the voltage offset, ΔV_{CC} , with the phase. The origin of this, which seems to be a systematic effect, is not yet understood and will be addressed in the future to fully characterise the behavior of the beam in the presence of a phase offset in the CC. It should be pointed out that the impact of this effect on the interpreting the CC noise induced emittance growth measurements is limited and thus it will not be a matter of concern for this thesis.

5 | Experimental studies 2018: emittance growth from Crab Cavity noise

In Chapter 3 the theoretical model for the transverse emittance growth caused by amplitude and phase noise in a CC was discussed. On September 5, 2018, a dedicated experiment was conducted in the SPS to benchmark this model against experimental data and confirm the analytical predictions. In particular, the idea was to inject artificial noise in the CC RF system and compare the measured emittance growth rates with the the theoretically computed ones. In this chapter the measurement results from the SPS are presented and discussed. The work published in Ref. [16] is the basis of this chapter.

Section ... describes the machine setup and the beam configuration for the emittance growth measurements. This includes a summary of the preparatory studies conducted in the previous years. In Section ...

5.1 Experimental configuration and procedure

This section gives an overview of the experimental setup and the procedure that was followed. First, it briefly discusses the preparatory studies that were performed during 2012-2017 [17, 18, 19], explaining the choice of the intensity and energy values for which the emittance growth measurements were conducted. Furthermore, it presents in detail the rest of the beam and machine conditions during the experiment. Last, the experimental procedure is explained.

5.1.1 Preparatory experimental studies

For studying the long-term emittance evolution a special mode of operation was set up in the SPS which is called "coast" (in other machines, it is referred to as storage ring mode) with bunched beams. In this mode, the bunches circulate in the machine at constant energy for long periods, from a few minutes up to several hours, similar to the HL-LHC case.

To make sure that the SPS can be used as a testbed for the emittance growth studies with CCs an extensive preparatory campaign was carried out through 2012-2017 [17, 18, 19]. The primary concern was the emittance growth that was observed in the machine from other sources than injected noise and will be referred to as the natural emittance growth in this thesis. The natural emittance growth needs to be well characterized and be kept sufficiently small in order to distinguish and understand the contribution from the CC noise.

From these studies, it was concluded that the optimal coast setup is at high energies, with low chromaticity and bunches of low intensity as it minimises the natural emittance growth [19]. The highest energy for which the SPS could operate in "coast" was 270 GeV and thus the experiments were performed at this energy. That limitation was introduced due to the rms power deposited in its magnets when operating at high energy for long period of time. Moreover, as the natural emittance growth was found to be a single bunch effect four bunches were used. That choice was made to reduce the statistical uncertainty of the measurements but not to increase the beam intensity.

5.1.2 Machine and beam configuration

During the experiment the Landau octupoles were switched off. Nevertheless, a residual non-linearity was present in the machine mainly due to multipole components in the dipole magnets [3, 4]. The transverse feedback system was also switched off. Unfortunately, no measurements of chromaticity are available from the day of the experiment. However it was ensured that the chromaticity was corrected to small positive values.

Last, only one CC, CC2, was used for simplicity and it operated at 1 MV. This value was validated with the HT monitor (post-processing procedure described in Chapter 4). Unfortunately, only one beam based measurement of the CC voltage is available which is displayed in Fig. 5.1. It is clear that the measured value of voltage amplitude, $V_{CC} = 0.99 \pm 0.04$ MV, is in good agreement with the requested one. It should be noted, that due to the beam energy of 270 GeV the crabbing is less visible than the example discussed in Chapter 4 (see Fig. 4.10) for 26 GeV. Therefore, here the part of the signal that is used for the fit is the one for which the normalised sum signal (black dashed line) is above 0.2 (instead of 0.4 that was the condition for the case of 26 GeV)



Figure 5.1: Demonstration of the sinusoidal fit on the HT monitor reading in order to obtain the CC parameters as described in Section 4.4. The fit results, are given in the yellow box. The measured voltage amplitude, V_{CC} , was found to be 0.99 MV while its uncertainty, ΔV_{CC} , was measured at 0.04 MV. The measured voltage value agrees well with the requested value of 1 MV.

The main machine and beam parameters used for the emittance growth measurements in 2018 are listed in Table 5.1.

Table 5.1: Main machine and beam parameters for the emittance growth studies with CCs in SPS in 2018.

Parameter	Value
Beam energy, E_b	270 GeV
Revolution frequency, f_{rev}	43.375 kHz
Main RF voltage / frequency, V_{RF} / f_{RF}	3.8 MV / 200.39 MHz
Horizontal / Vertical betatron tune, Q_x / Q_y	26.13 / 26.18
Horizontal / Vertical first order chromaticity, Q'_x / Q'_y	$\sim 1.0 / \sim 1.0$
Synchrotron tune, Q_s	0.0051
CC2 voltage / frequency, V_{CC} / f_{CC}	1 MV / 400.78 MHz
Number of protons per bunch, N_b	3×10^{10} p/b*
Number of bunches	4
Bunch spacing	524 ns
Rms bunch length, σ_t	1.8 ns*
Horizontal / Vertical normalised emittance, ϵ_x / ϵ_y	$2 \mu\text{m} / 2 \mu\text{m}^*$
Horizontal / Vertical rms tune spread, $\Delta Q_x^{rms} / \Delta Q_y^{rms}$	2 ns / 2 ns [†]

* The value correspond to the requested initial value at the start of each coast. The measured evolution of the parameter through the experiment is presented in the Sections 5.3 and 5.4.

[†] Here the rms betatron tune spread includes only the contribution from the amplitude detuning introduced by the multiple components in the SPS dipole magnets. The calculations for the listed values can be found in Appendix A.4.

5.1.3 Experimental procedure

The experiment took place on September 5, 2018, and was given a total time window of about 6 hours (start:~10:30, end:~17:00). In order to characterize the CC noise induced emittance growth, different levels of controlled noise were injected into its LLRF system and the bunch evolution was recorded for about 20-40 minutes (for each noise setting). The experiment was conducted over three coasts, since a new beam was injected every time the quality of the beam was seen to be degraded e.g. very large beam size. In the following, the different noise settings will be denoted as "Coast N -Setting M ", where N stands for the coast number and M for the different noise levels applied in each coast in chronological order. After the experiment, the measured growth rates would be compared with the theoretically expected values from the model described in Chapter 3.

5.2 Injected RF noise

The noise injected in the CC RF system was a mixture of amplitude and phase noise

up to 10 kHz, overlapping and primarily exciting the first betatron sideband at ~ 8 kHz. The phase noise was always dominant. The noise levels were measured with a spectrum analyzer E5052B [20] and are expressed as $10\log_{10} \mathcal{L}(f)$ [dBc/Hz]. The relation between the measured noise levels and the PSDs in Eq. (3.1) and Eq. (3.2) is given by $S_{\Delta} = 2\mathcal{L}(f)$, with $S_{\Delta A}$ in $1/\text{Hz}$ and $S_{\Delta\phi}$ in rad^2/Hz . This relation is extensively discussed in Appendix B and specifically in B.3. Figure 5.2 displays an example measurement of amplitude (left) and phase (right) noise acquired during the experiment.



Figure 5.2: Example amplitude (left) and phase (right) noise spectra measured with a spectrum analyzer E5052B [20] during the emittance growth studies with CCs in SPS. The noise spreads-out up to 10 kHz (grey dashed line) overlapping the first betatron sideband at ~ 8 kHz (green dashed line). The spikes at high frequencies correspond to the harmonics of the revolution frequency and are a result of the bunch crossing.

PSD values of interest

As already discussed in Chapter 3 the noise induced emittance growth depends on the noise power at the betatron and synchrobetatron sidebands for the phase and amplitude noise respectively (see Eq. (3.2) and Eq. (3.1)). Therefore, the noise power values of interest for this thesis are the ones at the first betatron $f_b = 0.18 \times f_{rev} = 7.82$ kHz and at the synchrobetatron sidebands at $f_b \pm Q_s \times f_{rev} = f_b \pm \sim 220$ kHz.

However, it can be clearly seen from Fig. 5.2 that the measured noise spectra are noisy: random changes in amplitude are observed from point to point within the signal. To this end, the PSD value at the first betatron sideband, f_b , is determined as the average of the PSD values over a frequency range of ± 500 Hz around it, while its uncertainty is considered to be the standard deviation over that range. In the

following, it is assumed for simplicity that the PSD at the synchrotron sidebands equals the PSD at the first betatron sideband as they lie very close to each other. At this point, it should be mentioned that the validity of these assumptions was tested with numerical simulations which used the measured spectra (Chapter 7).

The emittance growth measurements were performed with seven different noise levels. The values of the phase and amplitude noise for each setting are listed in Table 5.2.

Effective phase noise

In order to make a meaningful comparison between the different levels of noise, the concept of effective phase noise is introduced: this is the phase noise level that would lead to the same emittance growth as that from both phase and amplitude noise according to the theoretical model (Chapter 3).

For the calculation of the effective phase noise the averaged bunch length for each case is used (bunch length measurements at Section 5.4). The uncertainty on the effective phase noise is computed following the standard procedure of the propagation of the uncertainty (Appendix A.3). [Do I need to show all the calculations?](#). The calculated effective phase noise values for the experimental conditions are also listed in Table 5.2. The shown values correspond to the results using the parameters of the first bunch. However, the difference between the values for the other bunches is very small and is also within the displayed uncertainties. The noise levels mentioned in the following analysis of the experimental data correspond to the calculated effective phase noise.

5.3 Emittance growth measurments

This section presents the transverse emittance growth measurements with CC RF noise. It discusses first the measurement of the beam emittance with the SPS Wire Scanners (WS) and then it provides an overview of the emittance growth measurements for the four bunches over all the different noise settings.

5. Experimental studies 2018: emittance growth from Crab Cavity noise

Table 5.2: Phase and amplitude noise levels injected in the CC RF system for the emittance growth studies of 2018. The listed values correspond to the average PSD values over a frequency range of ± 500 Hz around the first betatron sideband, f_b . The calculated effective phase noise for the parameters of the first bunch are also listed.

	$10\log_{10}\mathcal{L}(f)$ [dBc/Hz]		
	Phase noise	Amplitude noise	Effective phase noise
Coast1-Setting1	-122.6 ± 0.6	-128.1 ± 0.6	-121.8 ± 0.5
Coast1-Setting2	-101.4 ± 0.8	-115.2 ± 0.6	-101.3 ± 0.8
Coast2-Setting1	-115.0 ± 0.8	-124.1 ± 0.5	-114.6 ± 0.7
Coast2-Setting2	-111.4 ± 0.6	-115.7 ± 0.4	-110.2 ± 0.5
Coast3-Setting1	-110.9 ± 0.9	-116.9 ± 0.4	-110.1 ± 0.8
Coast3-Setting2	-106.4 ± 0.3	-112.9 ± 0.6	-105.8 ± 0.3
Coast3-Setting3	-101.4 ± 0.7	-106.9 ± 0.5	-100.6 ± 0.6

5.3.1 SPS Wire Scanners

The SPS is equipped with Wire Scanners (WS) to measure the transverse beam emittance. The SPS WS system is described in detail in Ref. [21, 22]. For the SPS tests, the emittance was measured with WS both for the horizontal and vertical plane (BWS.51995.H and BWS.41677.V respectively).

The working principle is shown in Fig. 5.3. A thin wire rapidly moves across the proton beam and a shower of secondary particles is generated. The signal from the secondary particles is then detected by a system of scintillator and photomultiplier (PM) detectors outside of the beam pipe. By measuring the PM current as a function of wire position over multiple turns the transverse beam profile is reconstructed. An example of a vertical profile is shown in Fig. 5.4.

Fitting of transverse profiles

Assuming gaussian beams and for $u = x, y$ being the index that respectively corresponds to the horizontal and vertical plane, the rms beam size, σ_u , is obtained following the standard procedure of least squares fitting (see Appendix A.2). In particular, the measured beam profiles from each scan are fitted with the following four-parameter (A, k, μ, σ_u) gaussian function:

$$f(x) = k + Ae^{-\frac{(x-\mu)^2}{2\sigma_u^2}}, \quad (5.1)$$

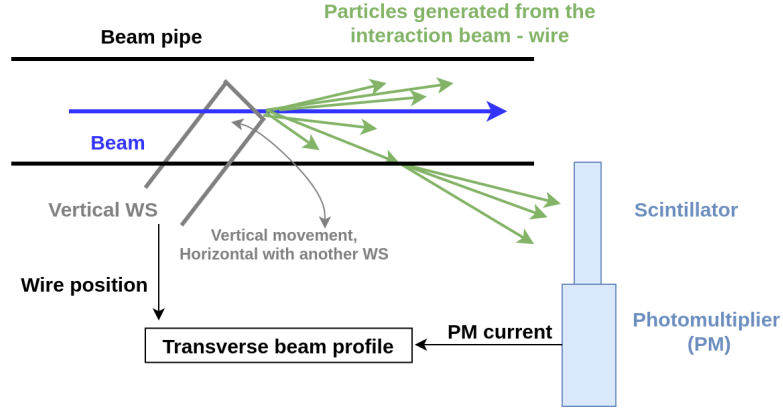


Figure 5.3: Sketch of the SPS rotational wire scanners [22]. The wire moves across the proton beam generating secondary particles which are then detecting by a scintillator and a photomultiplier. From the measured photomultiplier current the beam profile is reconstructed.

where k is the signal offset of the PM, A is the signal amplitude, μ is the mean of the Gaussian distribution and σ_u its standard deviation. The uncertainty of the measured rms beam size, $\Delta\sigma_u$, is defined as the error of the fit of the σ_u parameter (see Appendix A.2).

An example of the beam profile measured from the SPS WS at a specific time is shown in Fig. 5.4 (light blue dots) along with the gaussian fit (orange line).



Figure 5.4: Vertical beam profile obtained from the BWS.41677.V instrument. The measured data points (light blue) are fitted with a four parameter gaussian (orange) to obtain the beam size. The calculated emittance and its uncertainty are also shown.

Computing the normalised beam emittance

The formula for computing the normalised beam emittance from the beam size, σ_u is given by:

$$\epsilon_u = \frac{\sigma_u^2}{\beta_{u,WS}} \beta\gamma, \quad (5.2)$$

where σ_u is the rms beam size, $\beta_{u,WS}$ the beta function at the WS location and β, γ the relativistic parameters. Note that $u = x, y$ is the index that respectively corresponds to the horizontal and vertical plan.

Assuming that the relativistic parameters are free of error, the uncertainty of the computed emittance, $\Delta\epsilon_u$, depends on the uncertainty of the measured beam size, $\Delta\sigma_u$ and of the beta function at the location of the WS, $\Delta\beta_{u,WS}$, as follows:

$$\Delta\epsilon_u = \sqrt{\left(\frac{\partial\epsilon_u}{\partial\sigma_u}\right)^2 \Delta\sigma_u^2 + \left(\frac{\partial\epsilon_u}{\partial\beta_{u,WS}}\right)^2 \Delta\beta_{u,WS}^2} = \epsilon_u \sqrt{\left(\frac{2\Delta\sigma_u}{\sigma_u}\right)^2 + \left(\frac{\Delta\beta_{u,WS}}{\beta_{u,WS}}\right)^2}. \quad (5.3)$$

For the computation of the emittance values from the CC experiment of 2018, the following points were considered. First, in the 2018 SPS operational configuration, the dispersion was small at the WSs location and thus its contribution to the beam size was considered to be negligible¹. Moreover, for the studies at 270 GeV beam energy, $\beta\gamma$ equals 287.8 and the beta functions were 81.5 m and 62.96 m at the locations of the horizontal and vertical WS respectively. Last, the uncertainty on the beta functions at the location of the WS, $\Delta\beta_{u,WS}$, is 5% in both planes, which represents the rms beta-beating in the SPS [23].

Further considerations

It is worth noting here that during each measurement with the WS the beam profile is actually acquired twice as the wire crosses the beam in the forward direction (IN scan) and then in the reverse direction (OUT scan). For the 2018 measurements the emittance values obtained from IN and OUT scans, $\epsilon_{IN} \pm \Delta\epsilon_{IN}$ and $\epsilon_{OUT} \pm \Delta\epsilon_{OUT}$,

¹The dispersion at BWS.51995.H location in 2018 was $D_x = -15$ mm. At 270 GeV, the energy spread, δ , is of the order of 10^{-4} . Thus, from Eq. (2.3) the horizontal normalised emittance from the dispersion is expected at the order of 10^{-6} μm . Comparing to the observed beam size during the CC tests of a few microns the dispersion is negligible. **The measured D_x, D_y were found to be very small and thus their contribution is also considered negligible. The plan is to perform some measurements in 2022 to get a feeling of their values at the location of the wire scanners**

were found to be very similar. In the analysis of the 2018 measurements, the average emittance from the two scans, $\epsilon_{\text{avg}} = \langle \epsilon_{\text{IN}}, \epsilon_{\text{OUT}} \rangle$, is used. The uncertainty in the average, $\Delta\epsilon_{\text{avg},1}$, is given by [24]:

$$\Delta\epsilon_{\text{avg},1} = \frac{|\epsilon_{\text{IN}} - \epsilon_{\text{OUT}}|}{2\sqrt{2}}. \quad (5.4)$$

The propagated uncertainty from the measurement errors, $\Delta\epsilon_{\text{IN}}$ and $\Delta\epsilon_{\text{OUT}}$, is given by:

$$\Delta\epsilon_{\text{avg},2} = \frac{1}{2} \sqrt{\Delta\epsilon_{\text{IN}}^2 + \Delta\epsilon_{\text{OUT}}^2}. \quad (5.5)$$

Considering that $\Delta\epsilon_{\text{avg},1}$ and $\Delta\epsilon_{\text{avg},2}$ are independent, the combined uncertainty in the average, $\Delta\epsilon_{\text{avg}}$, is given by:

$$\Delta\epsilon_{\text{avg}} = \sqrt{\Delta\epsilon_{\text{avg},1}^2 + \Delta\epsilon_{\text{avg},2}^2}. \quad (5.6)$$

Finally, some emittance increase is expected during each wire scan, due to multiple Coulomb scattering. This effect has been extensively studied in Ref. [25]. For the rotational SPS WS and the energy of 270 GeV, at which the CC experiments were performed the expected emittance growth from the WS is expected to be between 0.0-0.2% per scan in both transverse planes. However, a conservative number of scans were carried out, ~ 20 scans per bunch and per plane during ~ 1 hour, in order to minimise the contribution from this effect.

5.3.2 Experimental results

In this section, an overview of the emittance growth measurements is presented. Figure 5.5 displays the bunch by bunch transverse emittance evolution through the total duration of the experiment. The three different coasts are distinguished in this plot with the blue dashed vertical lines. The values of the effective phase noise are also displayed (see Table 5.2), while the moments when the noise level changed are shown with the grey vertical lines. The four different colors (blue, orange, red, green) correspond to the four different bunches. For the bunches the notation "bunch N " will be used, where $N = \{1, 2, 3, 4\}$ according to their position in the bunch train. The errorbars of the emittance values correspond to the uncertainty computed using

Eq. 5.6. However, as they are very small comparing to the scale of the plots they are barely visible. Last, the emittance growth rates, $d\epsilon_u/dt$, for each setting and for each bunch are displayed at the bottom of each plot along with their uncertainties. The growth rates are obtained following the standard procedure of weighted least squares fitting (see Appendix A.2). In particular, the measured beam profiles from each scan are fitted with the following polynomial:

$$p(x) = c_0 + d\epsilon_u/dt \times t \quad (5.7)$$

where t is the time in seconds, $d\epsilon_u/dt$ the growth rate in meters per second and c_0 the constant offset in meters. The uncertainties of the growth rates correspond to the error of the fit (see Appendix A.2).

First observations and comments

Figure 5.5 demonstrates a clear emittance growth in the vertical plane which is expected due to the vertical CC. However, the CC noise is observed to induce growth also in the horizontal emittance as a result of residual coupling in the machine. Thus, the total emittance growth given by $d\epsilon_x/dt + d\epsilon_y/dt$ should be considered in the following. That was confirmed by PyHEADTAIL simulations [26] in the presence of CC RF noise and transverse coupling.

Furthermore, both the phase and amplitude noise levels for Coast1-Setting1 were found to be below noise floor of the instrument. Therefore, the transverse emittance growth observed during that case is a result of other sources (natural emittance growth, see Section 5.1.1) and will be considered as the background growth rate in the analysis below. [Is this approach ok? instead of using 0.45 and 0.55 um/h for the y and x planes respectively.](#)

Summary plot

Figure 5.6 provides a clearer view of the measurements presented in Fig. 5.5. It displays the measured emittance growth rates for each one of the four bunches for the different levels of injected noise. The horizontal error bars correspond to the uncertainty of the effective phase noise (see Section 5.2) while the vertical ones cor-

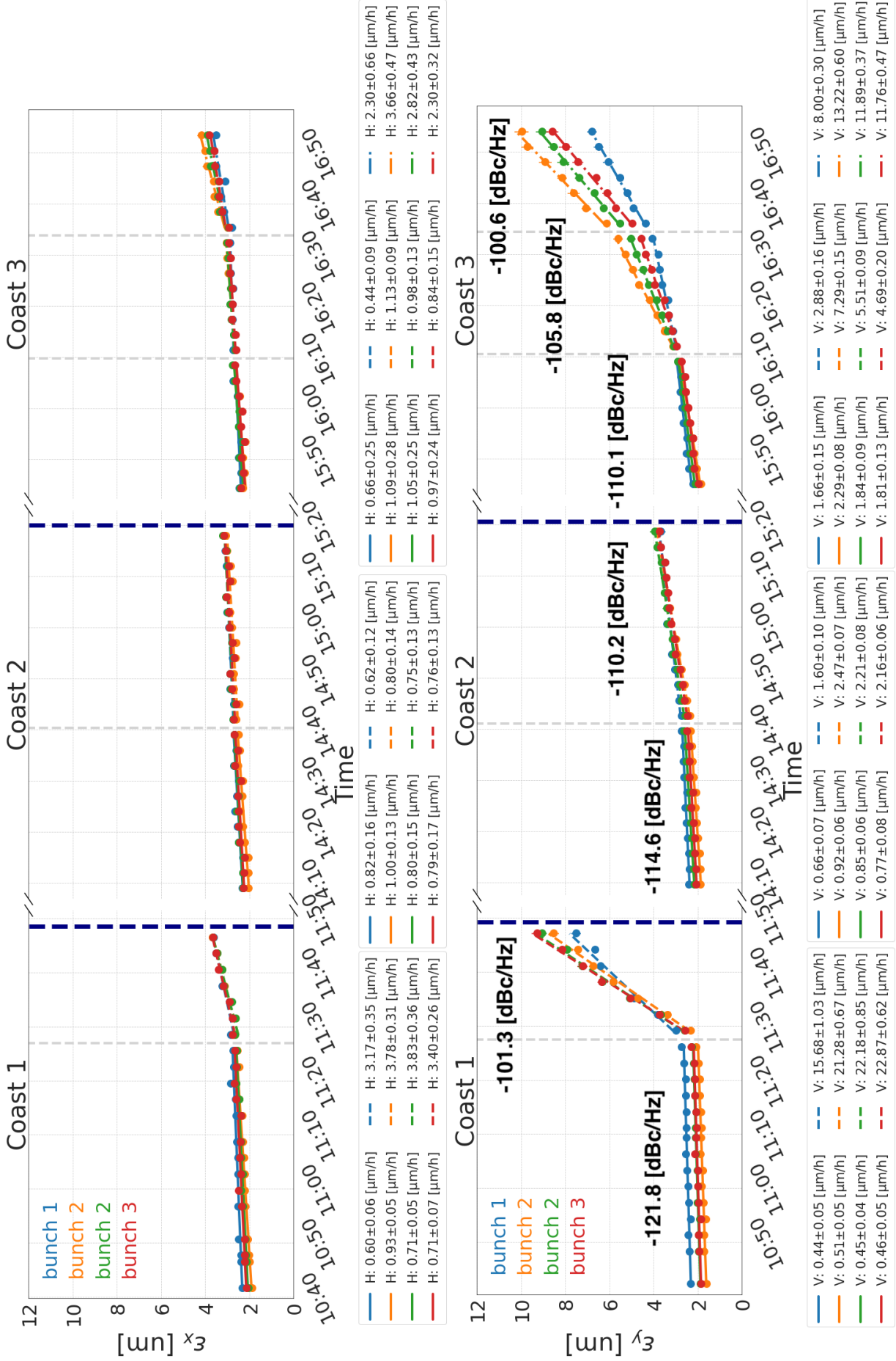


Figure 5.5: Bunch by bunch horizontal (top) and vertical (bottom) emittance evolution during the experiment on September, 15, 2018. The four different colors indicate the different bunches. The different applied noise levels are also shown while the moments when the noise level changed are indicated with the grey vertical dashed lines. The emittance growth rates along with their uncertainties for the seven different noise settings are displayed at the legend at the bottom of the plots.

respond to the uncertainty of the total transverse emittance growth calculated from the uncertainties of the horizontal and vertical growth rates following the standard procedure of the propagation of the uncertainty (Appendix A.3).



Figure 5.6: Summary plot of the emittance growth study with CC noise in 2018. The transverse emittance growth rate, for the four bunches, is shown as a function of the different levels of applied noise.

From the plot it becomes clear that the measured emittance growth was different for the four different bunches. Furthermore, the first bunch (blue) had systematically the smallest growth rate.

An attempt to understand these observations will be made in the following section by investigating a possible correlation between the transverse emittance growth and the beam evolution in the longitudinal plane.

5.4 Bunch length and intensity measurements

The measurements of the bunch length and intensity that took place in parallel with the emittance growth measurements are presented in this section. The goal is to get a more complete insight of the experimental conditions and possibly explain the different emittance growth rates observed for the four bunches which was discussed in the previous section. Initially, a short introduction on the instrument used for the measurements is provided. After that, the evolution of the longitudinal plane and of the intensity is analysed and discussed.

5.4.1 ABWLM and Wall Current Monitor

The bunch length was measured with two different instruments the ABWLM (A for RF, B for Beam, W for Wideband, L for Longitudinal, M for Measurement) [27] and the Wall Current Monitor [28]. Both ABWLM and Wall Current Monitor acquire the longitudinal bunch profiles, while ABWLM is much faster than the Wall Current Monitor. In the ABWLM case the bunch length is obtained by performing a gaussian fit on the acquired profiles. Only the calculated bunch length values are available but not the profiles themselves. For the case of the Wall Current Monitor the bunch length is estimated by computing the full width half maximum of the profiles and then using it to estimate the sigma of a gaussian distribution. The longitudinal profiles and the calculated bunch lengths are available for each acquisition. Furthermore, the Wall Current Monitor provides additional information on the relative bunch position with respect to the center of the RF bucket, which will also be used in the following analysis. No further details on the operation of these instruments are discussed here as the offline analysis was not performed by the author.

[How is the intensity calculated?](#)

5.4.2 Bunch length measurements

The bunch length measurements that took place during the CC noise induced emittance growth studies are shown in the bottom plot in Fig. 5.7. The small markers correspond to the data acquired with the ABWLM while the bigger markers to the data acquired with the Wall Current Monitor. The two upper plots contain the transverse emittance growth as discussed in Section 5.3.2. This is for easier comparison of the beam evolution in the transverse and in the longitudinal plane. The color code corresponds to the four different bunches.

Four main observations can be made. First, the plot demonstrates a very good agreement between the ABWLM and the Wall Current monitor. Second, an approximately bunch length increase of $\sim 9\%/h$ is observed for bunch 1 (blue) in all the three coasts. This rate, which is computed from the ABWLM data, is similar to the blow-up observed in the SPS for similar machine conditions [18]. Third, the bunch length increase for the last three bunches (2, 3, and 4) is larger compared to



Figure 5.7: Evolution of the beam in transverse and longitudinal planes during the CC noise induced emittance growth experiment. Top: Horizontal emittance growth measured with the SPS WS. Middle: Vertical emittance growth measured with the SPS WS. Bottom: Bunch length evolution measured with the ABWLM (small markers) and the Wall Current Monitor (bigger markers).

bunch 1. However, bunches 2, 3, and 4 seem to be longitudinally unstable as sudden jumps appear in their bunch length evolution and this could explain the faster bunch length increase. Last, no correlation is observed between the bunch length evolution and the change of noise level. In order to validate that bunches 2, 3, and 4 are unstable, the longitudinal profiles acquired with the Wall Current Monitor are studied in the next paragraph.

5.4.3 Longitudinal profile measurements

Two example longitudinal profile acquisitions from the Wall Current Monitor are discussed here as they can provide further insight on the sudden jumps observed in the bunch length values for bunches 2, 3, and 4. The selected acquisitions correspond to the moments where the sudden jumps are performed in the second and third coast and are shown in Fig 5.8. The relative bunch position with respect to the center of the RF bucket of each bunch for an acquisition period of 7 ms is also illustrated in the bottom plots of Fig. 5.8 for completeness.

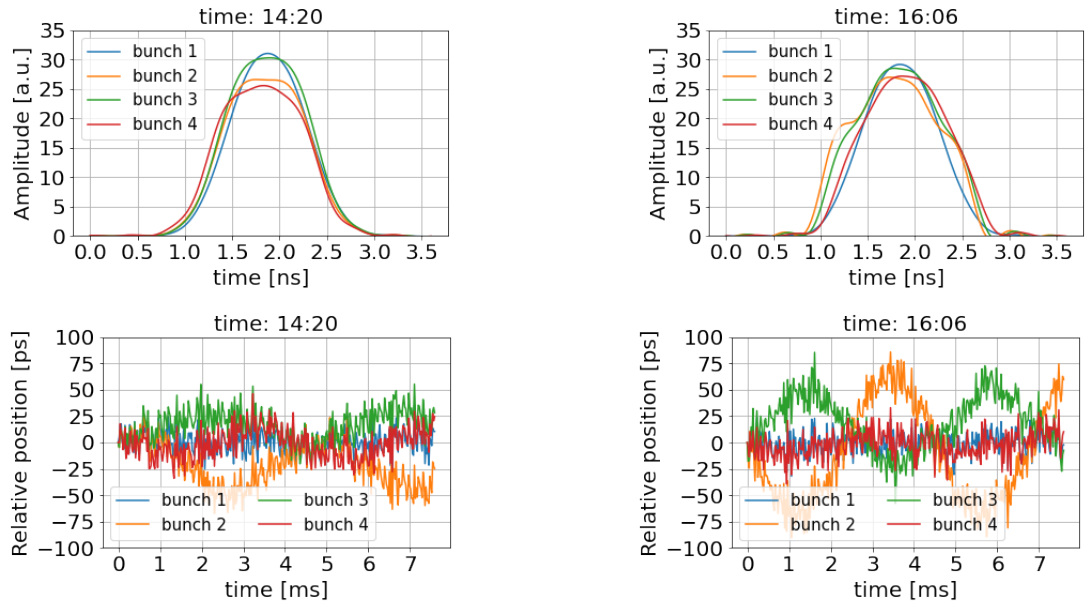


Figure 5.8: Longitudinal profiles (top) and relative bunch position with respect to the center of the RF bucket (bottom) acquired with the Wall Current Monitor. The acquisitions correspond to the times when the sudden jumps in the bunch length evolution are observed (see Fig. 5.7).

From Fig. 5.7, it becomes clear that bunches 2, 3, and 4 (orange, green, and red) are longitudinally unstable. This is believed to be due to the fact that the phase loop

was sampling only the first bunch because of the large bunch spacing of 525 ns [29]. For this reason, the following analysis is focused only on bunch 1, which was not affected by the instability. However, in the next paragraph the intensity measurements for all the four bunches are exceptionally illustrated.

5.4.4 Intensity measurements

The bunch by bunch intensity measurements that were performed along the experiment with artificial CC noise are displayed in Fig. 5.9. In particular the intensity values normalised with the initial value are shown for each bunch. The four different bunches are indicated with the four different colors. The acquisitions from both the ABWLM and the Wall Current Monitor are illustrated with the small and bigger markers respectively.

The following observations can be made. First, there is very good agreement between the measurements from the ABWLM and the Wall Current Monitor. Second, losses of $\sim 2\text{-}4\%$ /h, computed from the ABWLM acquisitions, are observed for bunch 1 (blue) in all the three coasts. This rate is even smaller of what was observed in the SPS in coast studies without external noise ($\sim 10\%$ /h) [18]. Last, more significant losses are observed for the longitudinally unstable bunches (bunch 2,3, and 4). However, this is not of concern as the last three bunches will not be included in the following analysis as discussed in the previous paragraph (5.4.3).

5.5 Comparison of measured transverse emittance growth with the theoretical predictions

This section, focuses on the main objective of the experiment which was the comparison of the measured transverse emittance growth with the expected values as computed from the theoretical model discussed in Chapter 3. As already discussed (Section 5.4.3), the comparison considers only bunch 1 as the other three bunches were found to be longitudinally unstable.

Figure 5.10 compares the measured (blue) and the theoretically calculated (black) emittance growth rates of bunch 1 for the different noise levels. For the comparison,

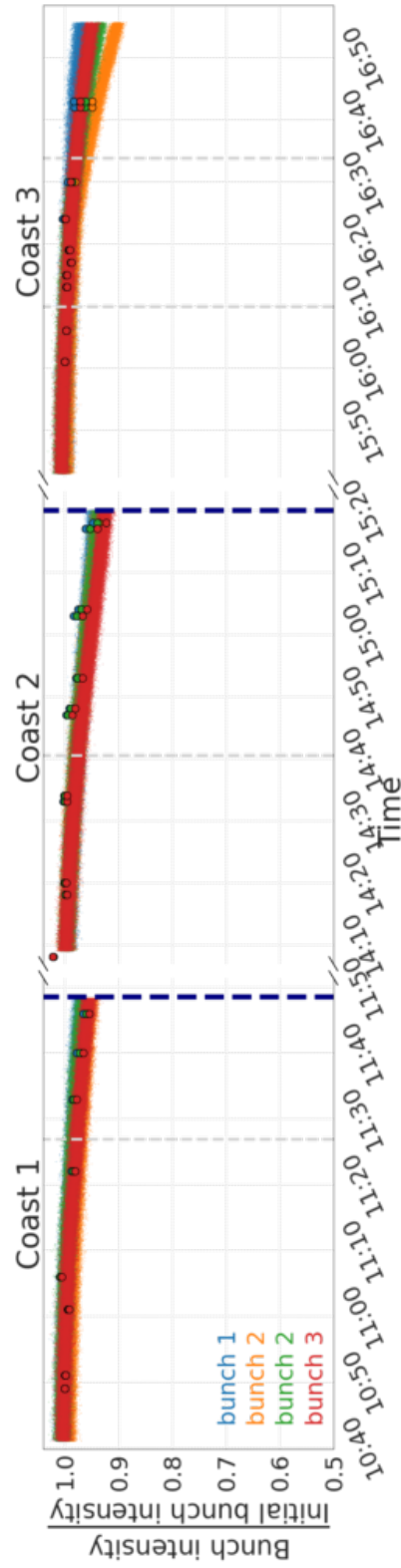


Figure 5.9: Intensity evolution as measured with ABLWM (smaller markers) and with the Wall Current Monitor (bigger markers) during the experiment with CC noise in 2018.

the background growth rate from other sources (measured during Coast1-Setting1, as discussed in Section 5.3) is subtracted from the measured values. In particular the background growth was measured $0.6 \mu\text{m}/\text{h}$ and $0.44 \mu\text{m}/\text{h}$ for the horizontal and vertical plane respectively. One should keep in mind that background subtraction has practically no impact for high noise levels. Instead, it is significant for small noise levels.

The expected emittance growth due to CC noise was estimate for all noise settings using Eq. (3.2). The growth was computed for the beam energy of 270 GeV, considering the vertical beta function at the location of the CC2 of 73.82 m and the revolution frequency of SPS which is 43.37 kHz. For each setting, the measured noise PSDs (i.e. effective phase noise) and the average bunch length over each observation window were used in the calculation. These values are listed in the first two columns of Table .. .

The horizontal error bars, for both measured and calculated growths, correspond to the uncertainty of the effective phase noise values (see Table 5.2). The vertical error bars for the measured growth are defined as the error of the linear fit on the emittance values (see Section 5.3). The vertical error bars on the theoretically calculated rates are computed following the standard procedure of propagation of the uncertainty. It should be mentioned here that only the uncertainties on the effective phase noise ($\sim 13\%$ on average for bunch 1) are included in the error propagation. The beam energy and the revolution frequency are assumed to be free of error, while the uncertainties of the rest of the parameters: bunch length, CC voltage and beta function ($\sim 2\%$, 0.01% , and 5% respectively) are not included as they are much smaller than those of the noise.

From Fig. 5.10 it becomes evident that the theory systematically overestimates the measured growth rates. The averaged discrepancy over all noise levels is a factor of 3: numerical values are given in Table ..

5.6 Conclusions and outlook

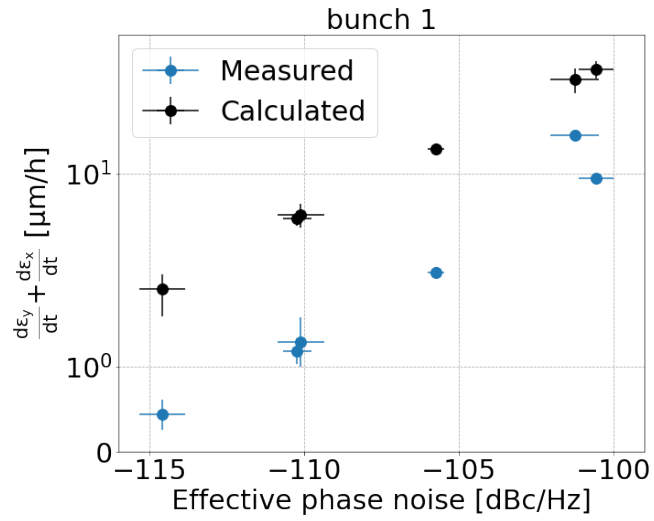


Figure 5.10: Summary plot of the emittance growth study with CC noise in 2018 focused on bunch 1 only. The measured emittance growth rate (blue) and the expected growths from the theoretical model (black) are shown as a function of the different levels of applied noise.

6 | Emittance growth studies 2018: Measurements and analysis

7 | Investigation of the discrepancy

7.1 Sensitivity studies

1. Sensitivity to how noisy is the noise spectrum 2. On the CC voltage 3. On the different bunch lengths.

7.2 Multiple errors

Contribution of the non-linearities with sixtracklib.

8 | Simple model of describing the decoherence suppression from impedance

9 | Application and impact for HL-LHC

10 | Conclusion

A | Definitions and methods of statistical analysis

A.1 Basic terminology

This appendix, introduces the basic terminology of statistical analysis and gives the definitions that are used in this thesis. The definitions follow the book by R. J. Barlow [30] where one can find a more detailed insight.

A.1.1 Averages

Arithmetic mean

For a data set of N data $\{x_1, x_2, x_3, \dots, x_N\}$ the arithmetic mean or just mean of the value of x is:

$$\langle x \rangle = \frac{1}{N} \sum_{i=1}^N x_i. \quad (\text{A.1})$$

Below, two properties of the arithmetic mean are discussed as they are used in this thesis.

- The mean of the sum of two variables x and y is equal to the sum of their means, ie:

$$\langle x + y \rangle = \langle x \rangle + \langle y \rangle \quad (\text{A.2})$$

- If x and y are independent the mean of their product equals:

$$\langle x \cdot y \rangle = \langle x \rangle \cdot \langle y \rangle \quad (\text{A.3})$$

Root mean square

In the classical definition in mathematics, the root mean square (rms) is an alternative to the arithmetic mean and is defined as:

$$x^{rms} = \sqrt{\frac{x_1^2 + x_2^2 + x_3^2 + \dots + x_N^2}{N}} = \langle x^2 \rangle. \quad (\text{A.4})$$

- **Disclaimer:** It is common in physics and in sciences in general for the term rms to correspond to what is actually defined as standard deviation (see definition in Appendix A.1.2). This convention, is also followed in this thesis.

A.1.2 Measuring the spread

Variance

For a data set of N data $\{x_1, x_2, x_3, \dots, x_N\}$ the variance of x expresses how much it can vary from the mean value, $\langle x \rangle$. The variance, $\text{Var}(x)$, is defined as:

$$\text{Var}(x) = \frac{1}{N} \sum_{i=1}^N (x_i - \langle x \rangle)^2. \quad (\text{A.5})$$

Alternatively, the variance can be expressed in a simpler way as follows (see Ref. [30] p.24-25):

$$\text{Var}(x) = \langle x^2 \rangle - \langle x \rangle^2. \quad (\text{A.6})$$

Standard deviation

The square root of the variance is the standard deviation (std):

$$\sigma_x = \sqrt{\text{Var}(x)} = \sqrt{\frac{1}{N} \sum_{i=1}^N (x_i - \langle x \rangle)^2}, \quad (\text{A.7})$$

or as follows from Eq. (A.6):

$$\sigma_x = \sqrt{\langle x^2 \rangle - \langle x \rangle^2}. \quad (\text{A.8})$$

The spread in a data set is usually expressed with the standard deviation instead of the variance, as the standard deviation has the same units with the variable x .

Full width half maximum

An alternative measure of the spread is the full width half maximum (FWHM).

A.1.3 Data sets with more than one variables - Covariance

In the case that each element of the data set consists of a pair of variables, $\{(x_1, y_1), (x_2, y_2), (x_3, y_3), \dots, (x_N, y_N)\}$ the covariance expresses the extent to which x and y tend to vary together. The covariance between x and y is defined as:

$$\text{Cov}(x, y) = \frac{1}{N} \sum_{i=1}^N (x_i - \langle x \rangle)(y_i - \langle y \rangle). \quad (\text{A.9})$$

It can be seen that the covariance of variable x with itself equals the variance. In particular, it is written:

$$\text{Cov}(x, x) = \sqrt{\frac{1}{N} \sum_{i=1}^N (x_i - \langle x \rangle)^2} = \text{Var}(x) = \sigma_x^2. \quad (\text{A.10})$$

A.2 Least squares fitting

In sciences, many quantities can not be measured directly but can be inferred from measured data by fitting a model function to them. Common model functions are the Gaussian, polynomial, or sinusoidal. The fitting procedure followed in this thesis is called "least squares" and is described below based on Ref. [31].

Suppose that we have N data points (x_i, y_i) and that $y = f(x, \alpha, \beta)$ is the model function that describes the relationship between the points. The objective of the fit is to determine the optimal parameters α, β such as the model function describes best the data points. This is done by minimising the χ^2 statistics with respect to α and β :

$$\chi^2 = \sum_{i=1}^N [y_i - f(x_i, \alpha, \beta)]^2, \quad (\text{A.11})$$

where y_i is the observed value and $f(x_i, \alpha, \beta)$ the expected value from the model. In other words, χ^2 is a measure of deviation between the measurement and the expected result, and thus its minimisation results in the best fit i.e. to the optimal parameters α, β .

Weighted least squares fitting

Suppose that we have N data points $(x_i, y_i \pm \Delta y_i)$, where Δy_i is the uncertainty of y_i ,

and that $y = f(x, \alpha, \beta)$ is the model function that describes the relationship between the points. To define the optimal parameters α, β taking into account the impact of the uncertainty Δy_i , Eq. (A.11) is written as:

$$\chi^2 = \sum_{i=1}^N \frac{[y_i - f(x_i, \alpha, \beta)]^2}{\Delta y_i^2} \quad (\text{A.12})$$

Error of the fit

The standard deviation of the fit results, $\sigma_\alpha, \sigma_\beta$, is estimated by the square root of the diagonal of their covariant matrix:

$$\begin{pmatrix} \sigma_\alpha^2 & \text{Cov}(\alpha, \beta) \\ \text{Cov}(\beta, \alpha) & \sigma_\beta^2 \end{pmatrix} \quad (\text{A.13})$$

In this thesis, the uncertainties of the fit results, $\Delta\alpha, \Delta\beta$, are defined as the standard deviation, σ_α and σ_β , of the corresponding optimal parameters.

The values of the optimal parameters and their covariance matrix are computed in this thesis using the `scipy.curve_fit` [32] function of the Python programming language.

A.3 Propagation of uncertainty

Suppose that y is related to N independent variables $\{x_1, x_2, \dots, x_N\}$ with the following function:

$$y = f(x_1, x_2, \dots, x_N). \quad (\text{A.14})$$

If $\{\Delta x_1, \Delta x_2, \dots, \Delta x_N\}$ the uncertainties of $\{x_1, x_2, \dots, x_N\}$ respectively, the uncertainty of y , is given by [30]:

$$\Delta y = \sqrt{\left(\frac{\partial f}{\partial x_1} \Delta x_1\right)^2 + \left(\frac{\partial f}{\partial x_2} \Delta x_2\right)^2 + \dots + \left(\frac{\partial f}{\partial x_N} \Delta x_N\right)^2} \quad (\text{A.15})$$

A.4 Detuning with amplitude

- The linear detuning is given by the following formula, for octupole components - write for detuning coefficients in the numerocultere - check sondre's thesis

The detuning with amplitude is computed by:

$$\Delta Q_x = 2(\alpha_{xx}J_x + \alpha_{xy}J_y) \quad (\text{A.16})$$

$$\Delta Q_y = 2(\alpha_{yy}J_y + \alpha_{yx}J_x) \quad (\text{A.17})$$

where α_{yy} , α_{xx} and $\alpha_{xy} = \alpha_{yx}$ are the detuning coefficients with units [1/m] and J_x , J_y the action variables.

Rms detuning with amplitude

From the definition of variance, the variance of the vertical amplitude detuning is given by:

$$\begin{aligned} \text{Var}(\Delta Q_y) &= \langle \Delta Q_y^2 \rangle - \langle \Delta Q_y \rangle^2 \\ &= \langle 2^2(\alpha_{yy}J_y + \alpha_{yx}J_x)^2 \rangle - \langle 2(\alpha_{yy}J_y + \alpha_{yx}J_x) \rangle^2 \\ &= 2^2 \left[\langle (\alpha_{yy}J_y + \alpha_{yx}J_x)^2 \rangle - \langle \alpha_{yy}J_y + \alpha_{yx}J_x \rangle^2 \right] \\ &= 2^2 \left[\langle (\alpha_{yy}J_y)^2 + 2\alpha_{yy}\alpha_{yx}J_yJ_x + (\alpha_{yx}J_x)^2 \rangle - (\langle \alpha_{yy}J_y \rangle + \langle \alpha_{yx}J_x \rangle)^2 \right] \\ &= 2^2 \left[\alpha_{yy}^2 \langle J_y^2 \rangle + 2\alpha_{yy}\alpha_{yx} \langle J_yJ_x \rangle + \alpha_{yx}^2 \langle J_x^2 \rangle - \alpha_{yy}^2 \langle J_y \rangle^2 - 2\alpha_{yy}\alpha_{yx} \langle J_y \rangle \langle J_x \rangle - \alpha_{yx}^2 \langle J_x \rangle^2 \right] \\ &= 2^2 \left[\alpha_{yy}^2 \langle J_y^2 \rangle + \cancel{2\alpha_{yy}\alpha_{yx} \langle J_yJ_x \rangle} + \alpha_{yx}^2 \langle J_x^2 \rangle - \alpha_{yy}^2 \langle J_y \rangle^2 - \cancel{2\alpha_{yy}\alpha_{yx} \langle J_yJ_x \rangle} - \alpha_{yx}^2 \langle J_x \rangle^2 \right] \\ &= 2^2 \left[\alpha_{yy}^2 (\langle J_y^2 \rangle - \langle J_y \rangle^2) + \alpha_{yx}^2 (\langle J_x^2 \rangle - \langle J_x \rangle^2) \right] \\ &= 2^2 \left[\alpha_{yy}^2 \text{Var}(J_y) + \alpha_{yx}^2 \text{Var}(J_x) \right] \end{aligned} \quad (\text{A.18})$$

In the development of Eq. A.18 the properties of the mean discussed in Eq. (A.2) and (A.3) are used.

Now, according to the definitions introduced in Appendix A.1, the root mean square

(rms) for the vertical amplitude detuning is written:

$$\begin{aligned}
 \Delta Q_y^{rms} &= \sigma_{\Delta Q_y} = \sqrt{\text{Var}(\Delta Q_y)} \\
 &= \sqrt{2^2 [\alpha_{yy}^2 \text{Var}(J_y) + \alpha_{yx}^2 \text{Var}(J_x)]} \\
 &= 2 \sqrt{\alpha_{yy}^2 (\sigma_{J_y})^2 + \alpha_{yx}^2 (\sigma_{J_x})^2} \\
 &= 2 \sqrt{[\alpha_{yy}(\sigma_{J_y})]^2 + [\alpha_{yx}(\sigma_{J_x})]^2}
 \end{aligned} \tag{A.19}$$

where σ_{J_y} and σ_{J_x} stand for the standard deviation of the action variables J_y and J_x respectively

The actions, J_x and J_y follow an exponential distribution (see Eq. (2.7)). It is known that for an exponential distribution the mean equals the standard deviation. Therefore, Eq. A.19 can be written as follows:

$$\Delta Q_y^{rms} = 2 \sqrt{[\alpha_{yy}\langle J_y \rangle]^2 + [\alpha_{yx}\langle J_x \rangle]^2}. \tag{A.20}$$

Following Eq. (2.6), the rms tune spread from amplitude detuning can be also written as:

$$\Delta Q_y^{rms} = 2 \sqrt{(\alpha_{yy}\epsilon_y^{geom})^2 + (\alpha_{yx}\epsilon_x^{geom})^2}. \tag{A.21}$$

Equivalently, the horizontal rms tune spread from amplitude detuning is given by:

$$\Delta Q_x^{rms} = 2 \sqrt{(\alpha_{xx}\epsilon_x^{geom})^2 + (\alpha_{yx}\epsilon_y^{geom})^2}. \tag{A.22}$$

Disclaimer: In the analysis presented above, the actions J_x and J_y refer to the initial distribution, for which they are actually independent. The actions later in time, are coupled due to the non-linear of the lattice.

Rms betatron tune spread from the SPS multiple errors at 270 GeV

Here the rms betatron tune spread from the SPS multipole components in the SPS dipole magnets is calculated for beam energy of 270 GeV. Using the values of the multipoles listed in Table 1.1 the corresponding detuning coefficients are obtained with MAD-X. In particular, $\alpha_{xx} = 148.39$ 1/m, $\alpha_{xy} = \alpha_{yx} = -402.91$ 1/m, $\alpha_{yy} = -48.7$ 1/m.

It should be noted that these values are obtained for zero linear chromaticity in both transverse planes.

The tune spread here is computed for the requested initial emittances for the emittance growth measurements of 2018 and 2021, $\epsilon_x = \epsilon_y = 2 \mu\text{m}$. Using Eq. (2.2) it can be seen that these values corresponds to geometric emittances of $\epsilon_x^{geom} = \epsilon_y^{geom} = 6.95 \text{ nm}$. By inserting these values of detuning coefficients and geometric emittances in Eq. Eq., the rms tune spread is found to be:

in horizontal and vertical plane respectvily.

B | Fundamentals of signal analysis and measurement

This appendix discusses the basic terminology of signal processing and gives the definitions which are used in this thesis. The focus is on Fourier transform and the power spectral density. First the most general mathematical definitions which concern signals continuous in time and with infinite time duration are discussed. Secondly, the definitions are given for signals sampled at a finite number of points, which are considered for the measurements and for the computational analysis. Furthermore, the quantities that are used most often for noise power spectrum measurements and their relationship to the mathematical definitions of the power spectral density are discussed. Finally, the way of applying a measured noise spectrum in numerical simulations is described.

B.1 Continuous-time analysis

Fourier transform

A physical process (or signal or time series) can be described in the time domain by a continuous function of time, e.g. $y(t)$, or else in the frequency domain, where the process is specified by giving its amplitude \hat{y} as a function of frequency, e.g. $\hat{y}(f)$ with $f \in (-\infty, +\infty)$. In other words, $y(t)$ and $\hat{y}(f)$ are essentially different representations of the same function. In general, $\hat{y}(f)$ can be a complex quantity, with the complex argument giving the phase of the component at the frequency f .

One can switch between these two representations using the Fourier transform method. In this thesis the Fourier transform of a time series $y(t)$, which will be denoted in this

document by \hat{y} , is defined as [33]:

$$\hat{y}(f) = \int_{-\infty}^{\infty} y(t) e^{-2\pi i t f} dt, \quad (\text{B.1})$$

where f stands for any real number. If the time is measured in seconds the frequency, f , is measured in hertz.

The inverse Fourier transform, which is used to re-create the signal from its spectrum, is defined as:

$$y(t) = \int_{-\infty}^{\infty} \hat{y}(f) e^{2\pi i t f} df. \quad (\text{B.2})$$

Power spectral density and total power

The power spectral density, $S_{yy}(f)$, of a signal (or a time series), $y(t)$, will be used extensively in this thesis: it describes the distribution of the power in a signal between its frequency components, and is defined as the Fourier transform of the autocorrelation function, $R_{yy}(t)$ [5]:

$$S_{yy}(f) = \hat{R}_{yy}(f) = \int_{-\infty}^{\infty} R_{yy}(\tau) e^{-2\pi i \tau f} d\tau. \quad (\text{B.3})$$

The continuous autocorrelation $R_{yy}(\tau)$ is defined as the continuous cross-correlation integral of $y(t)$ with itself, at lag τ [34]:

$$R_{yy}(\tau) = (y * y)(\tau) = \int_{-\infty}^{\infty} \bar{y}(t) y(t + \tau) dt, \quad (\text{B.4})$$

where $*$ denotes the convolution operation and $\bar{y}(t)$ represents the complex conjugate of $y(t)$.

According to the cross-correlation theorem [34]:

$$\hat{R}_{yy}(f) = \bar{\hat{y}}(f) \hat{y}(f) = |\hat{y}(f)|^2, \quad (\text{B.5})$$

where $\hat{y}(f)$ is the Fourier transform of the signal as defined in Eq. (B.1).

From Eq. (B.3) and Eq. (B.5) the power spectral density of a signal $y(t)$ can be simply

written as the square of its Fourier transform:

$$S_{yy}(f) = |\hat{y}(f)|^2, \quad (\text{B.6})$$

with $f \in (-\infty, +\infty)$.

B.2 Discrete-time analysis

Discrete-time signals

Figure B.1 shows a part of a continuous signal $y(t)$. As already mentioned, for the measurements and the computational analysis, signals (or time series) sampled at a finite number of points are considered. Such signals are called discrete-time signals and in most cases they are sampled at equal points in time. For example, in Figure B.1, it is assumed that the continuous signal, $y(t)$, is sampled at intervals Δt creating a set of N points. The length in time between the first and final sample is $T_{\text{sample}} = \frac{N-1}{N} T$, where $T = N\Delta t$.

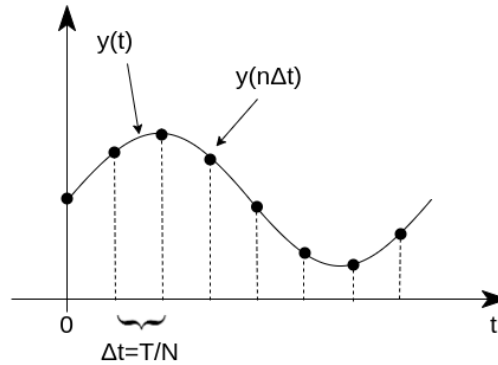


Figure B.1: Sampling of the continuous signal $y(t)$ at a finite number of points N . The sampled signal is the discrete-time signal $y(n\Delta t)$ with Δt the sampling interval and n an integer such that $n \in [0, N-1]$.

Discrete Fourier transform

Let us consider a discrete-time signal, y_n which is sampled at N consecutive samples, $y_n = y(n\Delta t)$, with $n \in [0, N-1]$ such that Δt is the sampling interval. For later convenience, we assume that N is an odd integer. As a first step, we note that the in-

tegral of Eq. (B.1) can be represented by a discrete sum in the limit that $\Delta t \rightarrow 0$:

$$\hat{y}(f) = \int_{-\infty}^{\infty} y(t) e^{-2\pi i f t} dt = \lim_{\Delta t \rightarrow 0} \sum_{n=-\infty}^{\infty} y(n\Delta t) e^{-2\pi i f n\Delta t} \Delta t. \quad (\text{B.7})$$

Based on the expression for the summation in Eq. (B.7), we define the discrete Fourier transform as follows:

$$\hat{y}_k = \sum_{n=0}^{N-1} y(n\Delta t) e^{-2\pi i \frac{kn}{N}}. \quad (\text{B.8})$$

Here, the index k is an integer in the range $-\frac{N-1}{2}$ to $\frac{N-1}{2}$. Each component \hat{y}_k of the discrete Fourier transform is related to the component $\hat{y}(f)$ of the continuous Fourier transform of $y(t)$, for $f = k/T$, in the limit $\Delta t \rightarrow 0$ and $N \rightarrow \infty$ (and where it is assumed that $y(t) = 0$ for $t < 0$ and for $t > T$).

It should be noted that the discrete Fourier transform is calculated only at integer values of k , and therefore for N samples the discrete Fourier transform will consist of N numbers. The components of the discrete Fourier transform are calculated at frequencies f_k that are integer multiples of $\Delta f = 1/T = f_s/N$, with $f_s = 1/\Delta t$ the sampling frequency. In that case, $f_k \in [-\frac{N-1}{2T}, \frac{N-1}{2T}]$. An example of a discrete Fourier transform is shown in Fig. B.2.

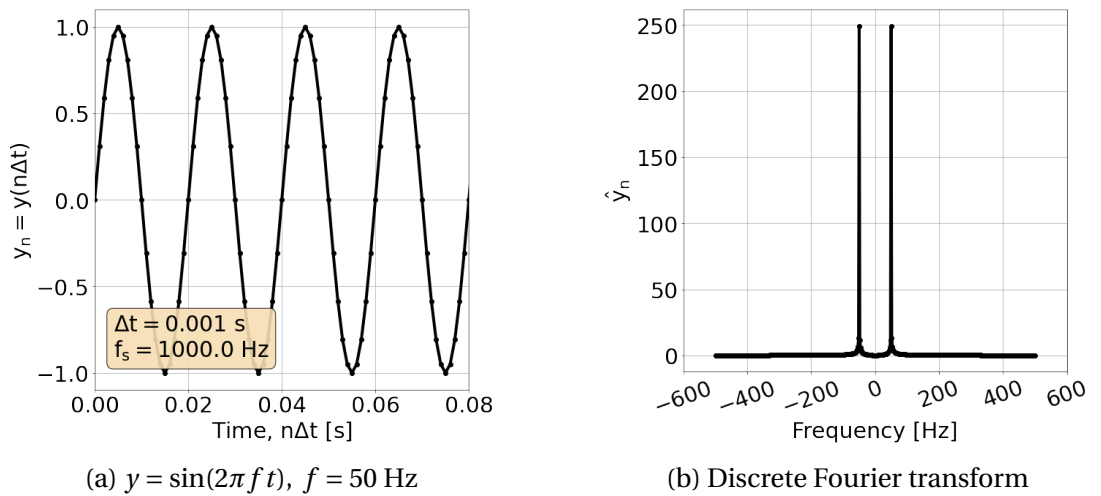


Figure B.2: Example of a signal sampled at discrete time intervals, and the corresponding discrete Fourier transform.

The inverse discrete Fourier transform is defined as:

$$y_n = y(n\Delta t) = \frac{1}{N} \sum_{k=-\frac{N-1}{2}}^{\frac{N-1}{2}} \hat{y}_k e^{2\pi i \frac{kn}{N}}, \quad (\text{B.9})$$

where $n \in [0, N-1]$ and where n and k are both integers.

The definitions given in Eq. (B.8) and Eq. (B.9) are consistent with those used in numpy, in the numpy.fft function [35] package of the Python programming language.

Power spectral density

Following Eq. (B.6) the power spectral density of a discrete-time signal should be estimated as follows:

$$S_{yy}(f_k) = A |\hat{y}_k(f_k)|^2, \quad (\text{B.10})$$

where $f_k \in [-\frac{N-1}{2T}, \frac{N-1}{2T}]$. A is a normalisation constant which is introduced in order to obtain the correct amplitudes at each frequency and thus the correct noise power. There are several different conventions for the choice of this normalization. In this thesis, the following normalization is considered (see more details in the dedicated paragraph at the end of this section):

$$S_{yy}(f_k) = \frac{1}{N^2 \Delta f} |\hat{y}_k(f_k)|^2, \quad (\text{B.11})$$

where $\Delta f = 1/T$ the frequency resolution and N the number of samples.

Figure B.3 shows an example power spectrum of the time-domain signal shown in Fig. B.2a. It can be seen that the spectrum that results from the analysis above is two-sided, which means that it has both positive and negative frequencies. It is also symmetric around the DC component ($f=0$ Hz), which is actually a property of a real signal.

The power spectral density is expressed in terms of the square of the amplitude of the signal per unit frequency. For example, for a signal defined in units of voltage, V, (e.g. from an oscillator) the units are V^2/Hz .

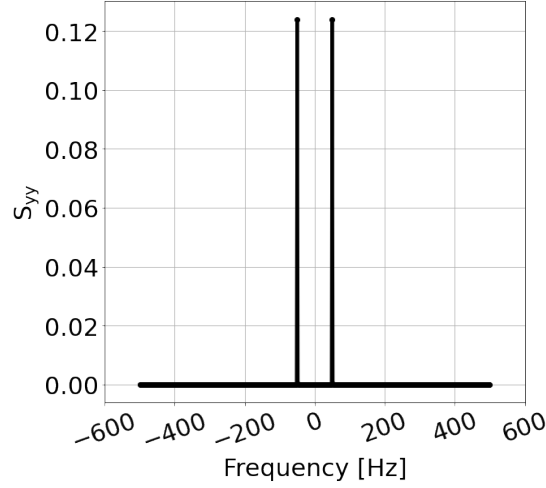


Figure B.3: Power spectrum of $y = \sin(2\pi f t)$, $f = 50$ Hz.

Conversion of a two-sided power spectrum to a single-sided power spectrum

As already mentioned, the frequency spectrum of a real signal is symmetric around the DC component and therefore the information contained in the negative frequency is redundant. For this reason, most of the instruments used in experiments to display a frequency analysis show just the positive part of the spectrum (single-sided spectrum).

In order to convert from a two-sided spectrum to a single-sided spectrum, the negative part of the spectrum is discarded, and the amplitudes of the positive frequency components (excluding the DC component, so for $f > 0$) are multiplied by a factor 2:

$$G_{yy}(f_k) = \begin{cases} 0, & f_k < 0 \\ S_{yy}(f_k), & f_k = 0 \\ 2S_{yy}(f_k), & f_k > 0 \end{cases} \quad (\text{B.12})$$

where $S_{yy}(f_k)$ is the two-sided spectrum and $G_{yy}(f_k)$ the single-sided spectrum. Figure B.4 illustrates the single-sided spectrum of the signal shown in Fig. B.2a.

Normalisation factor for the power spectral density of a discrete-time signal

This paragraph, discusses the choice of the normalisation factor $A = 1/(N^2 \Delta f)$ for the power spectral density of a discrete-time signal defined in Eq. (B.10):

$$S_{yy}(f_k) = A |\hat{y}_k(f_k)|^2. \quad (\text{B.13})$$

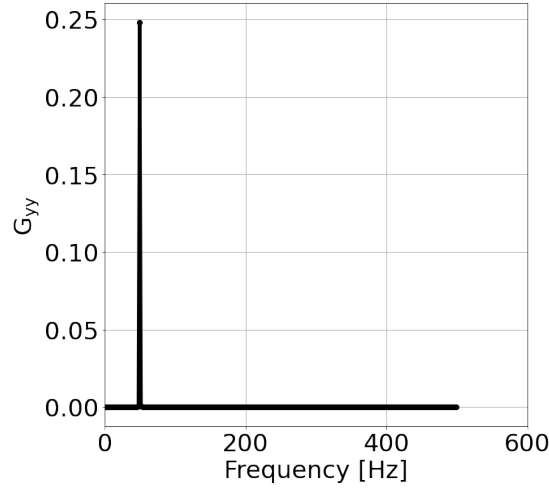


Figure B.4: Single-sided power spectrum of the signal shown in Fig. B.2(a).

Consider the example of a discrete-time series $y_n = y(n\Delta t)$ where n is an integer such that $n \in [0, N-1]$. y_n represents a sequence of successive points equally spaced in time, drawn from a normal distribution with known standard deviation σ and zero mean, $\mu = 0$. The variance of this collection of N equally spaced values is given by:

$$\sigma^2 = \frac{1}{N} \sum_{n=0}^{N-1} |y_n|^2. \quad (\text{B.14})$$

According to Parseval's theorem [34], the variance can be written as:

$$\sigma^2 = \frac{1}{N^2} \sum_{k=-\frac{N-1}{2}}^{\frac{N-1}{2}} |\hat{y}_k|^2, \quad (\text{B.15})$$

where \hat{y}_k is the discrete Fourier transform of y_n .

Using Eq. (B.3), the autocorrelation function $R_{yy}(\tau)$ for a continuous-time signal can be found from the inverse Fourier transform of $S_{yy}(f)$:

$$R_{yy}(\tau) = \int_{-\infty}^{\infty} \bar{y}(t)y(t+\tau) dt = \int_{-\infty}^{\infty} S_{yy}(f) e^{2\pi i f \tau} df. \quad (\text{B.16})$$

For zero lag, this becomes:

$$R_{yy}(0) = \int_{-\infty}^{\infty} S_{yy}(f) df = \sigma^2. \quad (\text{B.17})$$

This expresses the fact that the autocorrelation of a zero-mean stochastic process

(such as y_n) is equal to the variance. It should be noted here that this integration over the spectral components yields the total power of the process.

For a discrete-time signal, we require that the power spectral density $S_{yy}(f_k)$ corresponds to the power spectral density for the continuous-time signal. In that case, Eq. (B.17) becomes:

$$\sigma^2 = \sum_{k=-\frac{N-1}{2}}^{\frac{N-1}{2}} S_{yy}(f_k) \Delta f. \quad (\text{B.18})$$

From Eq. (B.15) and Eq. (B.18) this leads to:

$$\frac{1}{N^2} \sum_{k=-\frac{N-1}{2}}^{\frac{N-1}{2}} |\hat{y}_k|^2 = \sum_{k=-\frac{N-1}{2}}^{\frac{N-1}{2}} S_{yy}(f_k) \Delta f, \quad (\text{B.19})$$

and hence:

$$\sum_{k=-\frac{N-1}{2}}^{\frac{N-1}{2}} \frac{|\hat{y}_k|^2}{N^2 \Delta f} = \sum_{k=-\frac{N-1}{2}}^{\frac{N-1}{2}} S_{yy}(f_k). \quad (\text{B.20})$$

Therefore, to satisfy the requirement that the power spectral density for the discrete-time signal corresponds to that for the continuous-time signal, we define the power spectral density for a discrete-time signal:

$$S_{yy}(f_k) = \frac{|\hat{y}_k|^2}{N^2 \Delta f}. \quad (\text{B.21})$$

Hence, the normalisation factor in Eq. (B.10) is chosen to be:

$$A = \frac{1}{N^2 \Delta f}. \quad (\text{B.22})$$

B.3 Measuring amplitude and phase noise

Amplitude and phase modulation are two of the main types of noise in the output signal of an oscillator. The instantaneous output voltage of an ideal oscillator can be expressed as:

$$V(t) = V_0 \sin(2\pi f_0 t), \quad (\text{B.23})$$

where V_0 is the nominal peak voltage amplitude and f_0 the nominal frequency.

However, in practice, small inaccuracies will introduce amplitude and phase modulations. These modulations are included in the above signal by adding stochastic processes, represented by $\phi(t)$ and $\epsilon(t)$, as follows:

$$\begin{aligned} V(t) &= (V_0 + \epsilon(t)) \sin(2\pi f_0 t + \phi(t)), \\ &= \left(1 + \frac{\epsilon(t)}{V_0}\right) V_0 \sin(2\pi f_0 t + \phi(t)), \\ &= (1 + \alpha(t)) V_0 \sin(2\pi f_0 t + \phi(t)), \end{aligned} \quad (\text{B.24})$$

where $\phi(t)$ is the deviation from the nominal phase $2\pi f_0 t$, $\epsilon(t)$ is the deviation from the nominal amplitude and $\alpha(t) = \epsilon(t)/V_0$ is the normalised amplitude deviation. An example of a signal with phase and amplitude noise is shown in Fig. B.5.

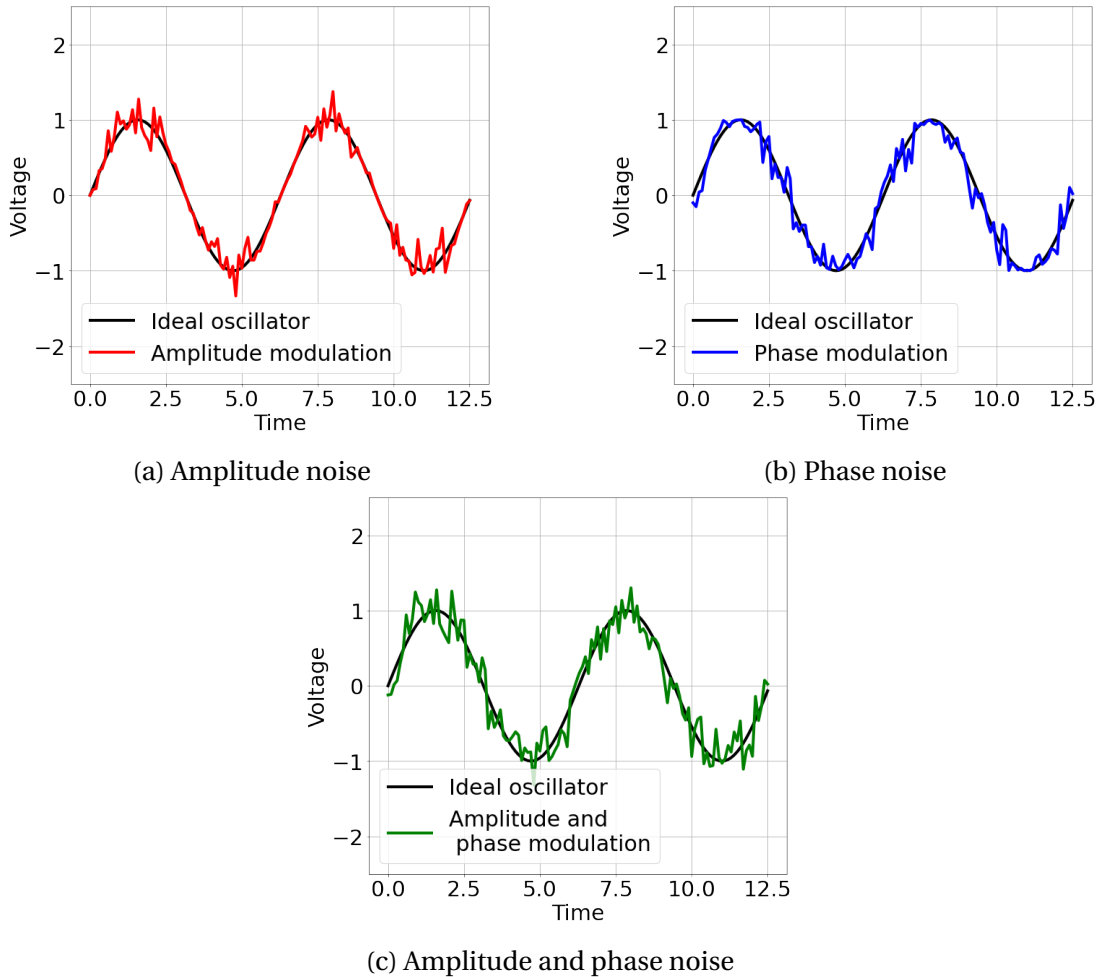


Figure B.5: Instantaneous voltage of an oscillator in the presence of (a) amplitude noise, (b) phase noise, and (c) both amplitude and phase noise.

Following the IEEE [36] conventions, the amplitude and phase modulation are measured by one-sided spectral densities, $G_{yy}(f)$. From Eq. (B.11) and Eq. (B.12), the

amount of amplitude noise can be expressed as:

$$G_\alpha(f_k) = 2S_A(f_k) = \frac{2}{N^2\Delta f} \left(\frac{|\hat{\epsilon}(f_k)|}{V_0} \right)^2 = \frac{2}{N^2\Delta f} |\hat{\alpha}(f_k)|^2, \quad (\text{B.25})$$

and the amount of phase noise can be expressed:

$$G_\phi(f_k) = 2S_\phi(f_k) = \frac{2}{N^2\Delta f} |\hat{\phi}(f_k)|^2, \quad (\text{B.26})$$

where f_k lies in a range of positive frequencies and $\hat{\alpha}(f_k)$ and $\hat{\phi}(f_k)$ are the discrete Fourier transforms of the modulation signals $\alpha(t)$ and $\phi(t)$ respectively. The units of the $G_\alpha(f_k)$ are V^2/Hz and the units of $G_\phi(f_k)$ are rad^2/Hz .

However, instruments used in experiments do not usually display directly the single-sided spectral density G_{yy} . Instead, the quantity $10\log_{10}\mathcal{L}(f_k)$ [dBc/Hz] is shown, with [36]:

$$\mathcal{L}(f_k) = G_{yy}(f_k)/2, \quad (\text{B.27})$$

where f_k ranges from 0 over the positive part of the spectrum. It should be emphasised that here \mathcal{L} is two-sided, as defined in [36], though it is considered that the instrument displays only the positive frequencies.

B.4 Applying a measured noise spectrum in numerical simulations

The goal of this section is to describe how one can convert the measured noise spectrum from a spectrum analyzer to a discrete time series that can be used for numerical simulations.

B.4.1 Crab cavity noise in numerical simulations

As follows from the discussion in section ??, phase and amplitude noise can be represented by discrete time series $\phi_n = \phi(n\Delta t)$ and $\alpha = \alpha(n\Delta t)$ respectively, so that the crab cavity (CC) instantaneous voltage is given by:

$$V_{CC}(n\Delta t) = V_0(1 + \alpha(n\Delta t)) \sin(2\pi f_0 n\Delta t + \phi(n\Delta t)), \quad (\text{B.28})$$

where V_0 and f_0 are the nominal crab cavity voltage and frequency respectively, $n \in [1, N - 1]$ and N is the number of samples.

In numerical simulations, N is taken to be equal to the number of turns in the simulation. The total time simulated is $T = N\Delta t$, where Δt is the sampling interval. Since the phase and amplitude noise are sequences of noise kicks which are applied to the CC voltage every turn, Δt is equal to the time needed for one turn around the machine. For the SPS, with a revolution frequency $f_{rev} = 43.38$ kHz, $\Delta t = 1/f_s = 1/f_{rev} \approx 23 \mu s$.

B.4.2 Measured noise spectrum

In the experiment performed in 2018, the amplitude and phase noise levels were measured with a spectrum analyser E5052B [20] and are expressed in terms of the quantity $10\log_{10} \mathcal{L}(f_k)$ [dBc/Hz] (see section ??). Figure B.6a shows an example of a phase noise spectrum acquired during the experiment, and which extends from 1 kHz to 10 MHz. The spectral lines observed at high frequencies correspond to harmonics of the revolution frequency.

B.4.3 Generating time series

In the following, the steps required to generate the discrete time series α_n and ϕ_n from the measured noise spectrum are discussed. The procedure involves converting the measured noise power to the two-sided power spectral density $S_\phi(f_k)$ and then using the inverse Fourier transform to produce the discrete-time series of noise kicks. In detail, the steps are as follows:

1. Convert the measured noise power $10\log_{10} \mathcal{L}(f_k)$ [dBc/Hz] to $G_\phi(f_k)$ [rad²/Hz] using Eq. (B.27) (Fig. B.6b).
2. Re-sample the noise spectrum. The measured noise power values are equally spaced in frequency on a logarithmic scale. A linear interpolation is needed such that they are equally spaced on a linear scale, every $\Delta f = f_s/N$. As already mentioned, since the beam encounters the crab cavities once each turn, $f_s = f_{rev}$ (= 43.38 kHz for the SPS). To this end, the linear interpolation extends up to $f_s/2$ as illustrated in Fig. B.6c. In our simulations, $N = 10^5$ turns are used.

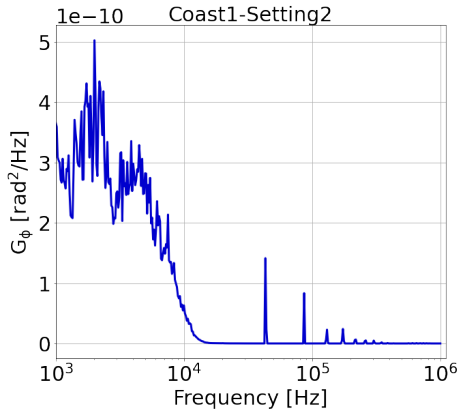
3. Create the positive spectral components of the two-sided power spectrum, S_ϕ , using Eq. (B.12) for $f_k > 0$. The result is shown in Fig. B.6d.
4. Compute the amplitude of the spectral components of the Fourier transform, $|\hat{\phi}_n(f_k)|$ according to Eq. (B.11). It should be noted, however, that this computation is done only for the positive part of the spectrum. Fig. B.6e depicts the result of this computation.
5. Generate the phase information for each positive spectral component. By definition the power spectral density does not contain any information about the phase of the frequency components. Therefore, one should generate this information by giving a random phase $\theta(f_k)$ obtained from uniform distribution between 0 and 2π .
6. Construct a one-sided frequency domain signal, $\hat{\phi}_n^{\text{os}}(f_k) = |\hat{\phi}_n(f_k)| e^{i\theta(f_k)}$. Once again this computation is done only for the positive spectral components, with $f_k \in \left[\Delta f, +\frac{f_s}{2}\right]$.
7. Construct the two-sided Fourier transform spectrum. First, create the negative components of the Fourier transform by taking the complex conjugate of the positive components. Furthermore, the information for the zero frequency component (DC) is missing from the measured spectrum, since this extends from 1 kHz to 10 MHz. In order to do the conversion correctly, the zero frequency term is set to 0, so that $\hat{y}_n(0) = 0$. The two-sided Fourier transform is then given by:

$$\hat{\phi}_n(f_k) = \begin{cases} |\hat{\phi}_n^{\text{os}}(f_k)| e^{i\theta(|f_k|)}, & f_k \in \left[-\frac{f_s}{2}, -\Delta f_s\right] \\ |\hat{\phi}_n^{\text{os}}(f_k)| = 0, & f_k = 0 \\ |\hat{\phi}_n^{\text{os}}(f_k)| e^{i\theta(|f_k|)}, & f_k \in \left[+\Delta f_s, +\frac{f_s}{2}\right] \end{cases} \quad (\text{B.29})$$

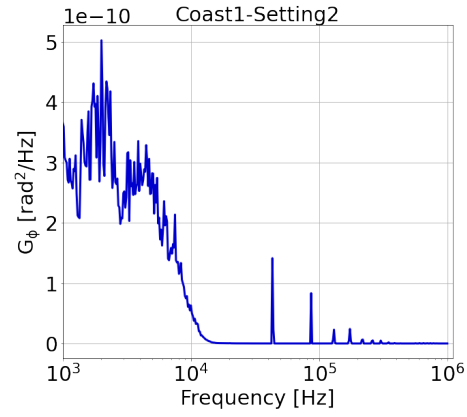
It is clear that $\hat{\phi}_n(f_k)$ has both positive and negative frequencies and the magnitude is symmetric in f_k .

8. Finally, apply the inverse Fourier transform, Eq. (B.9), to $\hat{\phi}_n(f_k)$. The output is a random discrete time series of N values sampled every $\Delta t = 1/f_s = 1/f_{rev}$. In other words, ϕ_n forms the sequence of noise kicks that will act on the particles

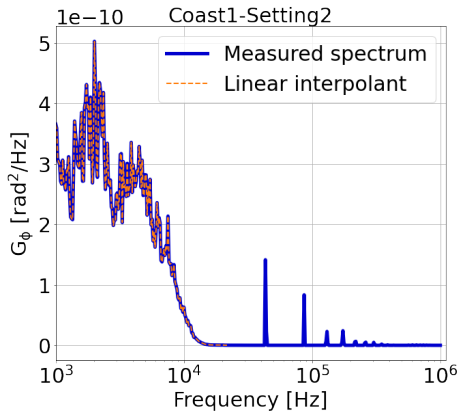
in the beam on each turn in the simulations.



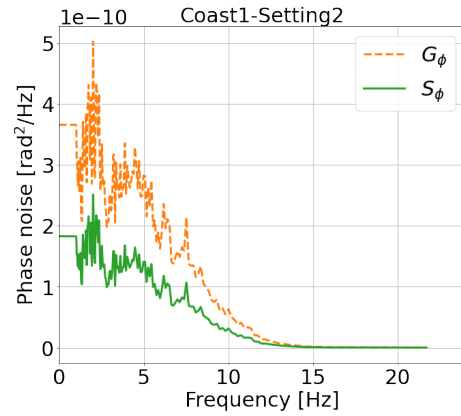
(a) Phase noise spectrum measured with a spectrum analyzer E5052B, in units dBc/Hz.



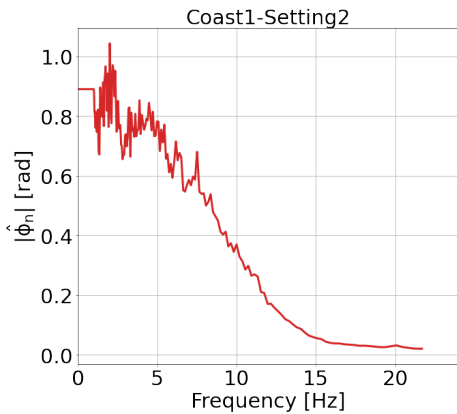
(b) Measured phase noise spectrum in units rad²/Hz.



(c) Linear interpolation of the measured noise spectrum.



(d) Positive spectral components of the two-sided power spectrum S_ϕ .



(e) Amplitudes of the spectral components of the Fourier transform.

Figure B.6: Steps required to generate the sequence of noise kicks to be applied in the simulations from the measured noise spectrum.

B.4.4 Validation of the time series reconstruction

This section describes the benchmarks that were carried out to ensure that the method described in section B.4.3 produces a valid time series for a set of noise kicks, for a given power spectrum.

Comparison of measured and reconstructed power spectrum

Figure B.7 shows the results of the first benchmark, comparing the measured power spectral density with the power spectral density computed from the generated time series ϕ_n . The two power spectra appear to be consistent with each other, which supports the validity of the method described above for generating the sequence of noise kicks from a given power spectrum.

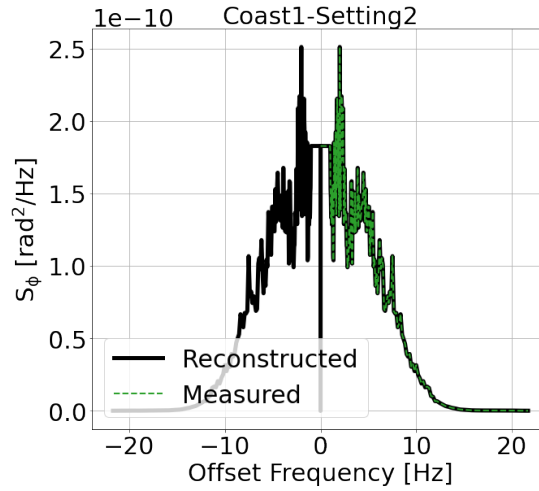


Figure B.7: Power spectral density computed from the time series ϕ_n produced from a measured power spectrum (black), compared with the original measured power spectrum (green).

PyHEADTAIL simulations

Another way to validate the method for producing a sequence of noise kicks from a measured power spectrum is to perform numerical simulations using the generated noise kicks, and compare the resulting emittance growth with the predictions from an analytical model [1].

In the simulations, which were performed with PyHEADTAIL, the beam was tracked for 10^5 turns which corresponds to about 2.5 s in the SPS. A kick representing the effect of the crab cavities was applied on each turn. The noise kicks that the beam

encounters every turn at the CC location were generated from the phase and amplitude noise spectra of from Coast1-Setting2 of 2018 (Fig. 5.2).

It should be noted, however, that the sequence of noise kicks includes a random factor through the set of random phases $\theta(f_k)$. To reduce the uncertainty in the results, multiple simulation runs were conducted. The set of random phases was regenerated randomly for each of 10 runs with a different seed each time. For each run, the initial bunch distribution was also regenerated randomly 3 times. The mean and the standard deviation of the emittance values obtained from the tracking were computed over all trials. The emittance growth rate was computed by performing a linear fit to the mean of the emittance values.

Figures B.8a and B.8b show the emittance growth for the case of amplitude noise and phase noise respectively. The emittance evolution in the presence of both types of noise is also illustrated in Fig. B.8c. The simulated emittance growth rates show very good agreement with the predictions from the analytical model. The results again support the validity of the method for generating a sequence of noise kicks from a measured noise power spectrum, described in section B.4.3.

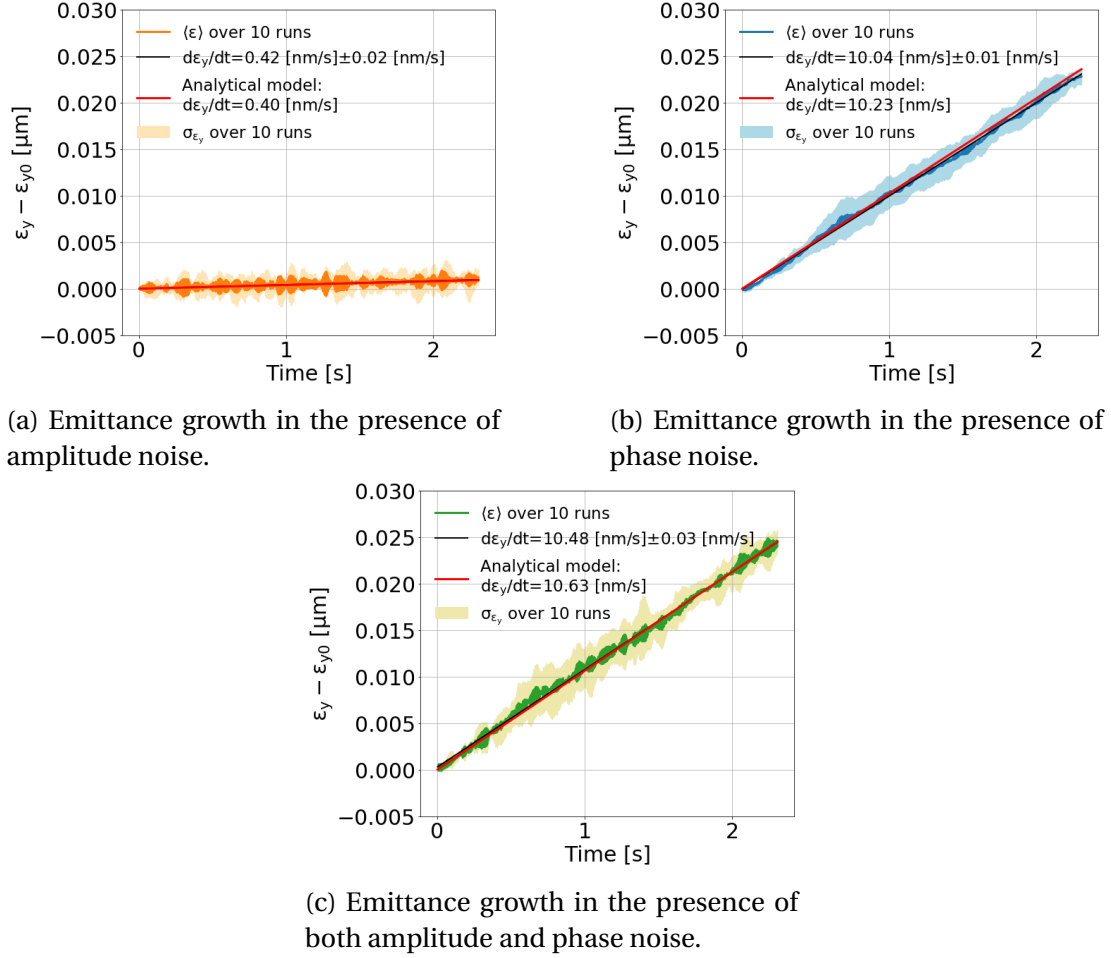


Figure B.8: Comparison between emittance growth found from simulations in Py-HEADTAIL and emittance growth expected from an analytical model [1]. The emittance growth is driven by amplitude and phase noise, with kicks in the simulations generated from a measured power spectrum.

C | Glossary and definitions

Peak to peak: Peak-to-peak (pk-pk) is the difference between the maximum positive and the maximum negative amplitudes of the wave.

<https://electronics.stackexchange.com/questions/313269/peak-to-peak-vs-amplitude>

Landau octupoles

Check the HL-LHC report to take ideas.

Bibliography

- [1] P. Baudrenghien and T. Mastoridis. “Transverse emittance growth due to rf noise in the high-luminosity LHC crab cavities”. In: *Phys. Rev. ST Accel. Beams* 18 (10 Oct. 2015), p. 101001. DOI: 10.1103/PhysRevSTAB.18.101001. URL: <https://link.aps.org/doi/10.1103/PhysRevSTAB.18.101001>.
- [2] *Official optics repository of the CERN Super Proton Synchrotron (official name SPS)*. Accessed: 16-2-2022. URL: <https://gitlab.cern.ch/acc-models/acc-models-sps/-/tree/2021/>.
- [3] Michele Carlà et al. “Studies of a New Optics With Intermediate Transition Energy as Alternative for High Intensity LHC Beams in the CERN SPS”. In: (2018), TUPAF022. 4 p. DOI: 10.18429/JACoW-IPAC2018-TUPAF022. URL: <https://cds.cern.ch/record/2664976>.
- [4] Androula Alekou et al. “SPS Long Term Stability Studies in the Presence of Crab Cavities and High Order Multipoles”. In: (2018), WEP2PO008. 3 p. DOI: 10.18429/JACoW-HB2018-WEP2PO008. URL: <https://cds.cern.ch/record/2640326>.
- [5] A. Papoulis. *Probability, Random Variables, and Stochastic Processes*. Communications and Signal Processing. McGraw-Hill, 1991. ISBN: 9780070484771. URL: <https://books.google.ch/books?id=4IwQAQAIAAJ>.
- [6] C. Zanoni et al. “The crab cavities cryomodule for SPS test”. In: 874 (July 2017), p. 012092. DOI: 10.1088/1742-6596/874/1/012092. URL: <https://doi.org/10.1088/1742-6596/874/1/012092>.
- [7] Rama Calaga, Ofelia Capatina, and Giovanna Vandoni. “The SPS Tests of the HL-LHC Crab Cavities”. In: (2018), TUPAF057. 4 p. DOI: 10.18429/JACoW-IPAC2018-TUPAF057. URL: <https://cds.cern.ch/record/2649807>.

- [8] P Baudrenghien et al. “Functional Specifications of the LHC Prototype Crab Cavity System”. In: (Feb. 2013). URL: <https://cds.cern.ch/record/1520896>.
- [9] Rama Calaga. *SPS Crab Cavity test RF Test Program*. Accessed: 11-11-2021. URL: <https://indico.cern.ch/event/718127/contributions/2951305/attachments/1645650/2629988/SPSCCtestv3.pdf>.
- [10] Carver Lee. *First proton beam dynamics results with crab cavities*. Accessed: 10-11-2021. URL: https://indico.cern.ch/event/800428/attachments/1804664/2945632/CrabCavity_BE_Seminar.pdf.
- [11] R. Jones and H. Schmickler. “The measurement of Q' and Q" in the CERN-SPS by head-tail phase shift analysis”. In: *PACS2001. Proceedings of the 2001 Particle Accelerator Conference (Cat. No.01CH37268)*. Vol. 1. 2001, 531–533 vol.1. DOI: 10.1109/PAC.2001.987561.
- [12] Thomas Levens, Kacper Łasocha, and Thibaut Lefèvre. “Recent Developments for Instability Monitoring at the LHC”. In: (2017), THAL02. 4 p. DOI: 10.18429/JACoW-IBIC2016-THAL02. URL: <https://cds.cern.ch/record/2313358>.
- [13] T. E. Levens et al. “Automatic detection of transverse beam instabilities in the Large Hadron Collider”. In: *Phys. Rev. Accel. Beams* 22 (11 Nov. 2019), p. 112803. DOI: 10.1103/PhysRevAccelBeams.22.112803. URL: <https://link.aps.org/doi/10.1103/PhysRevAccelBeams.22.112803>.
- [14] Tom Levens. *Beam instrumentation with SPS Crabs*. Accessed: 11-11-2021. URL: https://indico.cern.ch/event/718127/contributions/2951309/attachments/1646050/2630808/BI_SPS_Crabs.pdf.
- [15] Alexander Wu Chao et al. *Handbook of accelerator physics and engineering; 2nd ed.* Singapore: World Scientific, 2013. DOI: 10.1142/8543. URL: <https://cds.cern.ch/record/1490001>.
- [16] Natalia Triantafyllou et al. “Investigation of Damping Effects of the Crab Cavity Noise Induced Emittance Growth”. In: *12th International Particle Accelerator Conference*. Aug. 2021. DOI: 10.18429/JACoW-IPAC2021-TUPAB256.
- [17] R Calaga et al. “Proton-beam emittance growth in SPS coasts”. In: *Conf. Proc. C1205201* (May 2012), THPPP007. 3 p. URL: <https://cds.cern.ch/record/1451286>.

- [18] A Alekou et al. *Emittance growth in coast in the SPS*. Accessed: 26-11-2021. URL: https://indico.cern.ch/event/609486/contributions/2457542/attachments/1433340/2318716/EmittanceEvolutionCoastSPS_2017_April.pdf.
- [19] Fanouria Antoniou et al. "Emittance Growth in Coast in the SPS at CERN". In: *J. Phys.: Conf. Ser.* 1067 (2018), MOPMF061. 7 p. DOI: 10.18429/JACoW-IPAC2018-MOPMF061. URL: <https://cds.cern.ch/record/2649815>.
- [20] K. Gheen. *Phase Noise Measurement Methods and Techniques*. Accessed November 5, 2020. Agilent Technologies. URL: <https://studylib.net/doc/18034081/phase-noise-measurements>.
- [21] J. Bosser et al. "Transverse emittance measurement with a rapid wire scanner at the CERN SPS". In: *Nuclear Instruments and Methods in Physics Research Section A: Accelerators, Spectrometers, Detectors and Associated Equipment* 235.3 (1985), pp. 475–480. ISSN: 0168-9002. DOI: [https://doi.org/10.1016/0168-9002\(85\)90096-8](https://doi.org/10.1016/0168-9002(85)90096-8). URL: <https://www.sciencedirect.com/science/article/pii/0168900285900968>.
- [22] OE Berrig et al. *CERN-SPS Wire Scanner Impedance and Wire Heating Studies*. Tech. rep. Geneva: CERN, Sept. 2014. URL: <https://cds.cern.ch/record/1972478>.
- [23] Rogelio Tomas et al. "Improved algorithms to determine the non-linear optics model of the SPS from non-linear chromaticity". In: July 2007, pp. 4231–4233. ISBN: 978-1-4244-0916-7. DOI: 10.1109/PAC.2007.4439986.
- [24] Department of Physics University of Pennsylvania and Lab manual astronomy. *Managing errors and uncertainties*. Accessed: 18-03-2022. URL: <https://www.physics.upenn.edu/sites/default/files/Managing%20Errors%20and%20Uncertainty.pdf>.
- [25] Federico Roncarolo. "Accuracy of the Transverse Emittance Measurements of the CERN Large Hadron Collider". Presented 2005. 2005. URL: <https://cds.cern.ch/record/1481835>.
- [26] Philippe Baudrenghien. *LLRF experience for SPS & HL-LHC Outlook*. Accessed: 11-11-2021. URL: <https://indico.cern.ch/event/787363/contributions/3367294/attachments/1865644/3067685/HL-LHC19v6.pdf>.

- [27] F. Follin G. Papotti. *Online bunch length measurement for SPS OP*. Accessed: 26-11-2021. URL: https://indico.cern.ch/event/774525/contributions/3218683/attachments/1756129/2847423/20181120_LIUSPSBD.pdf.
- [28] G. Papotti. “A Beam Quality Monitor for LHC Beams in the SPS”. In: (Sept. 2008), 4 p. URL: <https://cds.cern.ch/record/1124099>.
- [29] T. Argyropoulos. *Private communication, Nov 2020*.
- [30] R. J. Barlow. *Statistics. A Guide to the Use of Statistical Methods in the Physical Sciences*. Manchester Physics Series. Wiley, 2013. ISBN: 9781118723234. URL: <https://liverpool.idm.oclc.org/login?url=https://search.ebscohost.com/login.aspx?direct=true&db=cat00003a&AN=lvb.b3130057&site=eds-live&scope=site>.
- [31] K. K. Gan. *Chi Square Distribution (χ^2) and Least Squares fitting*. Accessed: 03-03-2022. URL: <https://www.asc.ohio-state.edu/gan.1/teaching/spring04/Chapter6.pdf>.
- [32] *SciPy API Documentation*. Accessed: 16-2-2022. URL: https://docs.scipy.org/doc/scipy/reference/generated/scipy.optimize.curve_fit.html.
- [33] William H. Press et al. *Numerical Recipes: The Art of Scientific Computing*. 3rd ed. USA: Cambridge University Press, 2007. ISBN: 0521880688. URL: http://www.e-maxx-ru.lgb.ru/bookz/files/numerical_recipes.pdf.
- [34] R. Bracewel. *The Fourier Transform and its Applications*. 2nd ed. McGraw-Hill, 1986.
- [35] NumPy Project and Community. *NumPy API Documentation*. Accessed November 5, 2020. URL: <https://numpy.org/doc/stable/reference/routines.fft.html>.
- [36] “IEEE Standard Definitions of Physical Quantities for Fundamental Frequency and Time Metrology—Random Instabilities”. In: *IEEE Std Std 1139-2008* (2009), pp. c1–35. DOI: 10.1109/IEEESTD.2008.4797525.